

Internal Variability of an Energy-Balance Model with Delayed Albedo Effects

K. BHATTACHARYA¹

NASA Institute for Space Studies, Goddard Space Flight Center, New York 10025

M. GHIL

Courant Institute of Mathematical Sciences, New York University, New York 10012

I. L. VULIS

Department of Geological Sciences, Columbia University, New York 10027

(Manuscript received 17 August 1981, in final form 29 March 1982)

ABSTRACT

We present a simple, deterministic energy-balance model with possible relevance to climatic variations on the time scale of glaciation cycles. The lag between ice-sheet extent and zonally-averaged temperature is modeled as a time delay in the ice-albedo feedback. The model exhibits self-sustained oscillations which are quasi-periodic or aperiodic in character. Fourier spectra of solutions have the features of many paleoclimatic records: peaks of variable height and width superimposed on a continuous, red-noise type background.

1. Introduction

The phenomena of glacial-interglacial fluctuations have received the attention of geoscientists for a long time (Imbrie and Imbrie, 1979). Until recently, efforts toward understanding these fluctuations were constrained by a variety of limitations; among them, probably the most important one was the absence of continuous, reliable climatic records of these fluctuations. Recent studies on deep-sea sedimentation cores (e.g., Hays *et al.*, 1976) and ice cores from Greenland (e.g., Dansgaard *et al.*, 1971) have regenerated interest in the earth's glaciation history. This interest has been accentuated by the increasing preoccupation with the subject of terrestrial climate changes on various time scales.

One widely held view has been that the earth's climate changes with time, due to variations in factors external to the climatic system, i.e., "external conditions." Among the various explanations that fall into this class, the astronomical theory of glacial-interglacial oscillations (Milankovitch, 1941, *i.a.*) has attracted considerable attention. This theory holds that quasi-periodic changes in the parameters governing the earth's orbit in the solar system induce spatial and temporal changes in the seasonal cycle of solar radiation received at the earth's surface.

These changes, in turn, bring about the alternation of glacial and interglacial climates. The variations in insolation received at the earth's surface can be calculated from the relatively well-known perturbations in the terrestrial orbit. Therefore, this hypothesis can be studied in quantitative detail in relation to the temperature and ice volume history observed from the cores.

The astronomical insolation variations and the proxy records of climatic variables have been found to be in partial agreement with each other (Hays *et al.*, 1976). The proven agreement is mostly of an indirect, circumstantial nature. It is necessary to postulate some nonlinearity in the climatic system to explain the differences between the spectra of the input and output functions. It appears that, among the various physically reasonable possibilities, the glaciers themselves can be a source of such nonlinearity (Birchfield and Weertman, 1978). Considering the presently available evidence, the astronomical hypothesis appears to explain a significant part of the total climatic variability present over the time scales of 10^4 – 10^5 years.

The full spectrum of observed climatic variability (e.g., Kutzbach and Bryson, 1974), over all time scales, shows that the astronomical hypothesis accounts at best for only three peaks in the spectrum: at $\sim 20\,000$, $40\,000$ and possibly $100\,000$ years. A major part of the climatic variability is still to be explained. Many other hypotheses have been offered

¹ Present Affiliation: M/A COM Sigma Data Service Corp., Institute for Space Studies, 2880 Broadway, New York 10025.

to account for the continuous part of the variability spectrum, as well as other peaks (Ghil, 1981b). In particular, the study of high-sedimentation-rate cores from the North Atlantic has documented a strong peak in the $\delta^{18}\text{O}$ proxy record, which correlates well with global ice volume, close to 10 000 years, and a smaller peak with the same location in sea-surface temperature (Ruddiman and McIntyre, 1981). Similar results (Duplessy *et al.*, 1981) have been obtained on a possible peak in $\delta^{18}\text{O}$ and sea-surface temperature at 4000 years, and evidence exists for a climatic variability peak at 2500 years. It has also been proposed that anthropogenic sources can cause changes in terrestrial climate on shorter time scales.

In this work, the possible contribution of internal causes to terrestrial climatic change for long time scales is explored. Specifically, a one-dimensional energy-balance model is used to investigate the role of *almost-intransitivity* in earth's climate change. Lorenz (1970) noted that the different components of the earth's climatic system can store and release energy over widely different time scales. Nonlinear interactions between these components can give rise, therefore, to fluctuations in climatic variables on some of these time scales. Such self-sustaining fluctuations, in the absence of external changes, were termed almost intransitive. In the present model, the interacting components with different relaxation times are the cryosphere and the hydrosphere. The time scales of interest are 10^3 – 10^5 years. The results, however, could be indicative of the possibility and relevance of almost-intransitive behavior for the climatic system on other time scales.

In Section 2, the model is described. Section 3 discusses the model's steady-state solutions and their stability. Time-dependent solutions are studied in Section 4, which gives our main results. Discussion and conclusions follow in Section 5. Two Appendices outline the numerical methods used in the computations, and the spectral analysis of model solutions.

2. The model

The model used in the present work is an energy-balance model of the Sellers (1969) type. It is based on the model of Ghil (1976), which will be called the G model. The present model will be referred to as the BG model. Other versions of the model appear in Bhattacharya (1979), Bhattacharya and Ghil (1978) and Ghil and Bhattacharya (1979). (In these preliminary publications, the present model was called Model 2a, while the G model was called Model O.) To put our results in context, a brief description of the G model is given first, after which the BG model is described.

The G model (Ghil, 1976) is a zonally and vertically averaged mean annual energy-balance model. Sea-level temperature T is the only dependent vari-

able. The independent variables are time t and a scaled co-latitude x . Symmetry about the equator is assumed. The governing equation, which is an equation for energy balance at the Earth's surface, is of the form

$$C(x) \frac{\partial T(x, t)}{\partial t} = R_i[x, T(x, t)] - R_o[T(x, t)] + D \left[x, t, \frac{\partial T}{\partial x}(x, t), \frac{\partial^2 T}{\partial x^2}(x, t) \right], \quad (1a)$$

where $x = 2\phi/\pi$, ϕ being the co-latitude. Thus, at the pole, $x = 0$; at the equator, $x = 1$.

In Eq. (1a), $C(x)$ is the zonally averaged heat capacity of the Earth; it is determined from existing data. The absorbed part, R_i , of the incoming solar radiation is of the form

$$R_i = \mu Q(x) \{1 - \alpha[x, T(x, t)]\}. \quad (1b)$$

Here $Q(x)$ is the meridional distribution of incident solar radiation, while α is the albedo (reflectivity) of the earth's surface; $\mu = 1$ corresponds to present-day radiation conditions, while $\mu \neq 1$ corresponds to a change from such conditions. Thus μ gives the fractional change in the "solar constant."

The outgoing infrared radiation R_o , the part of energy lost to space, is

$$R_o = c [T(x, t)] \cdot \sigma \cdot [T(x, t)]^4, \quad (1c)$$

where σ is the Stefan-Boltzmann constant and c the emissivity coefficient.

The heat D transported along the earth's surface by conduction and convection is represented in the model by a diffusive approximation

$$D = \frac{1}{\sin \phi} \frac{\partial}{\partial \phi} [\sin \phi \cdot k(\phi)] \frac{\partial T}{\partial \phi}, \quad \phi = \frac{\pi}{2} x, \quad (1d)$$

where $k(\phi)$ is an eddy diffusivity that models both atmospheric and oceanic sensible heat fluxes, as well as atmospheric latent heat fluxes, in a manner to be described later on.

This form of one-dimensional energy-balance model, governed by Eqs. (1a)–(1d), was first proposed by Sellers (1969). The coefficients and forcing terms in these equations are the annual averages of the corresponding quantities.

The albedo in (1b) has the functional form

$$\alpha = \{b(x) - c_1[T_m + (T - c_2 z(x) - T_m)_-]\}_c. \quad (2a)$$

The meaning of the subscripts $()_-$ and $\{ \}_c$ is given for a generic quantity h by

$$h_- = \min\{h, 0\}, \quad (2b)$$

$$h_c = \begin{cases} 0.25, & h < 0.25 \\ h, & 0.25 < h < 0.85 \\ 0.85, & 0.85 < h. \end{cases} \quad (2c)$$

The cutoff implied in Eq. (2c) arises from the fact that snow and ice have the highest albedo ($\alpha = 0.85$ on the average), whereas bare ground and water have the lowest albedo ($\alpha = 0.25$ on the average).

The most striking feature of Sellers-type models is the piecewise linear dependence of albedo α on the elevated ground temperature $T - c_2 z(x)$. Albedo decreases monotonically within the limiting temperatures set by the cut-off values of the albedo. Values of these limiting temperatures depend on latitude due to the latitude-dependence of $b(x)$ and $z(x)$ in (2a). Eq. (2a) further states that when ground temperature is greater than T_m , no snow or ice is present, and the albedo is given by the bare-ground albedo.

The albedo as given by (2a) is planetary albedo, from satellite observations (Sellers, 1969). Sellers (1969) used the coefficients $b(x)$ to fit the meridional distribution of observed albedo; therefore the value of the albedo as given by (2a) is exact for the present distribution of surface temperatures. Eq. (2a) attempts to model the dependence of planetary albedo on surface temperatures different from the present ones. It includes, however, only the ice-albedo feedback, although several other albedo-feedback effects (e.g., due to cloud, vegetation, etc.) are conceivable.

The emissivity coefficient $c[T(x, t)]$ in Eq. (1c) was parameterized by Sellers (1969) as

$$c = 1 - m \tanh(c_3 T^6). \quad (2d)$$

This variable emissivity expresses empirically the "greenhouse effect"; i.e., the process by which outgoing longwave radiation is partly screened by various atmospheric gaseous absorbers and clouds. The expression (2d) indicates that as temperature increases, c decreases, i.e., the greenhouse effect becomes stronger.

The function $k(\phi)$ in Eq. (1d) has the form

$$k(\phi) = k_1(\phi) + k_2(\phi)g(\tilde{T}), \quad (2e)$$

$$g(\tilde{T}) = \frac{c_4}{\tilde{T}^2} \exp(-c_5/\tilde{T}),$$

where $\tilde{T}(x)$ is the present observed climate, from now on called "data climate;" $k_1(\phi)T_\phi$ is the combined sensible heat flux in atmosphere and ocean; and $k_2(\phi)g(\tilde{T})T_\phi$ is the latent heat flux in the atmosphere where $k_1(\phi)$ and $k_2(\phi)$ are eddy diffusivities. This particular formulation of k represented by Eq. (2e) makes the diffusive approximation [Eq. (1d)] a linear approximation; we shall not consider here nonlinear formulations, $k = k(\phi, T, T_\phi)$ (cf. Gal-Chen and Schneider, 1976; here $T_\phi = \partial T/\partial \phi$).

The functions $C(x)$, $Q(x)$ and $z(x)$ are determined directly from observations of the corresponding physical quantities. Like function $b(x)$, the constants c_1 and c_2 were also determined by fitting the existing planetary albedo data to Eq. (2a). The constants m

and c_3 were computed by Sellers (1969) by fitting data from current longwave radiation measurements to formulas (1c) and (2d). The form of the function $g(T)$ and the constants c_4 , c_5 appearing in (2e) are based on the thermodynamics of wet air and on empirical data (Berry *et al.*, 1945). The functions $k_1(\phi)$ and $k_2(\phi)$ are computed from measured data on sensible and latent heat flux, $k_1(\phi)T_\phi$ and $k_2(\phi)g(\tilde{T})T_\phi$, respectively.

The values of $C(x)$, $Q(x)$, $b(x)$, $z(x)$, $k_1(x)$ and $k_2(x)$ that were used for the G model are given in Table 1. The values of the constants are:

$$\left. \begin{aligned} c_1 &= 0.009, \quad c_2 = 0.0065 \text{ K m}^{-1} \\ c_3 &= 1.9 \times 10^{-15} \text{ K}^{-6} \\ c_4 &= 1.489 \times 10^9 \times 10^3 \text{ dyn K cm}^{-2} \\ c_5 &= 5350 \text{ K} \\ \sigma &= 1.356 \times 10^{-2} \text{ cal cm}^2 \text{ s}^{-1} \text{ K}^{-4} \\ m &= 0.5, \quad T_m = 283.16 \text{ K} \end{aligned} \right\} \quad (3)$$

Eq. (1a), together with relations (1b)–(1d) and (2a)–(2e) is a nonlinear, parabolic, partial differential equation of the form

$$C(x)T_t = \left(\frac{2}{\pi}\right)^2 \frac{1}{\sin(\pi x/2)} \frac{\partial}{\partial x} [\sin(\pi x/2)k(x)T_x(x)]$$

$$- [1 - m \tanh(c_3 T^6)]\sigma T^4 + \mu Q(x)\{1 - b(x) + c_1[T_m + (T - c_2 z(x) - T_m)_-]\}_c, \quad (4)$$

where $T_t = \partial T/\partial t$ and $T_x = \partial T/\partial x$. It has to be solved subject to the boundary conditions

$$T_x(0, t) = T_x(1, t) = 0, \quad (5a,b)$$

and to the initial condition

$$T(x, 0) = \tilde{T}(x). \quad (5c)$$

Eqs. (4)–(5) are the basis of the G Model. With minor modifications, they are the equations for the BG model as well.

The present (BG) model is obtained by introducing two changes in the temporal structure and one change in the spatial structure of the G model. The first change which affects the temporal behavior of the model was to use a new set of values for the heat capacity, $C = C_d(x)$, valid for very long climatic time scales. These values were based on the assumption that, on the time scales of interest, 10^3 – 10^5 years, convective overturning extends the effect of solar radiation all the way to the bottom of the oceans.

To compute the new heat capacity $C_d(x)$ the surface of the hemisphere is represented by a 5° latitude $\times 10^\circ$ longitude grid. For each box, the fractions of the surface area covered by land, ocean and ice are determined by using two recent data sets: one is the

TABLE 1. Empirical functions appearing in Eqs. (1), (2) and (4) (after Ghil, 1976).

Colatitude ϕ (deg)	\bar{T} (K)	C ($10^8 \text{ J m}^{-2} \text{ K}^{-1}$)	Q ($10^3 \text{ J m}^{-2} \text{ s}^{-1}$)	b	z (m)	k_1 ($10^3 \text{ J K}^{-1} \text{ m}^{-2} \text{ s}^{-1}$)	k_2 ($10^{-6} \text{ J N s}^{-1}$)
0	247.3625	0.2094	0.1784				
5				2.192	1204.5	0.1973	0
10	252.0740	0.4187	0.1842				
15				2.960	820.0	0.2595	0.3900
20	262.5715	0.6280	0.2026				
25				2.934	295.0	0.5022	0.8278
30	271.2980	1.9784	0.2424				
35				2.914	150.5	0.6289	1.4382
40	278.9325	2.3552	0.2914				
45				2.915	193.5	0.6325	2.0230
50	285.7530	2.4335	0.3366				
55				2.868	301.0	0.7100	1.5642
60	291.4090	2.4339	0.3743				
65				2.821	261.0	0.8472	0.2890
70	296.0815	2.3552	0.4024				
75				2.804	133.5	1.3424	-1.0635
80	298.7815	2.5122	0.4200				
85				2.805	156.0	2.0114	-4.4372
90	299.3510	2.3552	0.4258				

topography data set compiled by Gates and Nelson (1975), the other is the climatological surface temperature data set compiled by Alexander and Mobley (1974). In calculating the "deep-ocean" heat capacity $C_d(x)$, the penetration depths of solar radiation in land and ice are set to zero and the ocean depths are directly obtained from the topography data set of Gates and Nelson (1975). The mass of ocean water for each grid box is then computed using the known values of density for ocean water. This mass is in turn multiplied by the specific heat of ocean water to obtain the energy that is needed to heat up the area inside the grid box by 1 K. Upon dividing this energy by the area of the grid box, the result obtained is the surface heat capacity for this particular grid box. These surface heat capacities are averaged over a latitude circle to get the surface heat capacity of that particular latitude. Table 2 lists the values of C_d as a function of colatitude. As for the functions in Table 1 (cf. Ghil, 1976), they correspond to an average of the Northern and the Southern Hemisphere values at the same latitude.

TABLE 2. Values of the "deep ocean" heat capacity C_d , as function of colatitude ϕ .

	Colatitude (deg)				
	0	10	20	30	40
$C_d (10^{10} \text{ J m}^{-2} \text{ K}^{-1})$	0.6636	0.2952	0.4170	0.9421	1.0459
	Colatitude (deg)				
	50	60	70	80	90
$C_d (10^{10} \text{ J m}^{-2} \text{ K}^{-1})$	1.2222	1.1464	1.1577	1.2176	1.1992

The only change made in the spatial structure of the G model consists of modifying the albedo-temperature parameterization given by Eqs. (2a)–(2c). The original equation includes only the ice-albedo feedback according to Sellers' (1969) parameterization. Of the various other physical factors that contribute to the Earth's albedo-temperature feedback, cloudiness is generally thought to be the most important. Investigators in the field of climate modelling at every level of complexity have repeatedly emphasized the need for an adequate parameterization of cloud amount in terms of climatological variables. However, successful inclusion of cloud effects in the albedo-temperature parameterization has so far turned out to be an elusive goal. Many studies of dependence of cloudiness on temperature have been made, such as the observational ones of Cess (1976) and the theoretical ones of Schneider (1972), Paltridge (1974) and Temkin *et al.* (1975), among others.

In the present work, a very simple and crude cloud parameterization is attempted. Specifically, the *hypothesis* is made that in a certain range of surface temperature just above that corresponding to the permanently ice-covered ground, the albedo attains again a certain high value; for surface temperatures both larger and smaller than the limits of this range, the albedo is smaller. This hypothesis is based on the idea that, near the ice margin, steeper temperature gradients engender increased baroclinic activity, and hence more cloudiness. Observational and synoptical work of Lamb (1955), of Namias (1964, 1978) and of Schwerdtfeger and Kachelhoffer (1973) provide support for this hypothesis. Evidence for a close relationship between ice margin and the track of maximum cyclone frequency was recently summarized

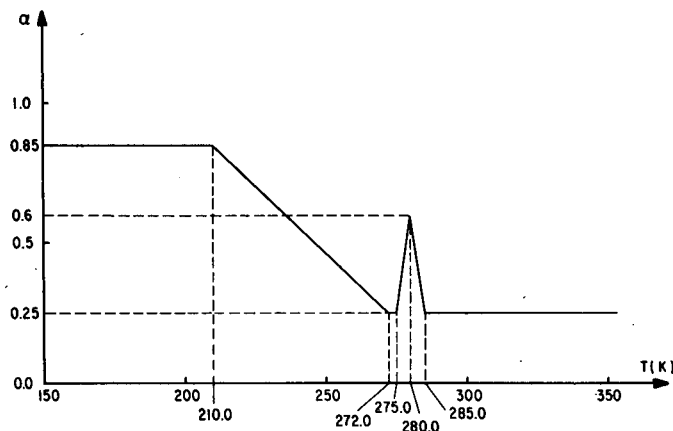


FIG. 1. Temperature-albedo parameterization used in the model. The hypothetical "kink" near 280 K is meant to represent the net climatic effect of increased cloud albedo due to intense baroclinic activity in the variable storm tracks near the ice margin.

by Goody (1980). In our parameterization, the higher cloud albedo over the baroclinically active band then compensates for the decrease in ground albedo over a certain temperature interval.

It is clear that the storm track will affect outgoing radiation, as well as the reflection of incoming radiation. The greenhouse effect of clouds, however, is already included in the original Sellers parameterization [Eq. (2d)], while the possible effect of clouds on albedo was not included in the Sellers (1969) model or the original G model. Many additional effects on albedo, such as that of vegetation (e.g., Cess, 1978), have not been included in the following parameterization; they are certainly important and should be investigated as soon and as thoroughly as possible.

To simplify the ensuing parameterization of the cloudiness effect on albedo, the dependence of the albedo on latitude, represented by the terms $b(x)$ and $z(x)$ in Eq. (2a), is eliminated. In the present model, $b(x)$ and $z(x)$ in (2a) are replaced by two constant quantities, \bar{b} and \bar{z} : $\bar{b} = 2.848$ and $\bar{z} = 249.7$ m. These values are obtained by area-averaging the original Sellers (1969) values of $b(x)$ and $z(x)$, as given in Table 1. With this change, the albedo-temperature parameterization becomes the same for all latitudes. The values of c_1 , c_3 and m also have to be adjusted slightly. The new values are: $c_1 = 0.0096$, $c_3 = 1.415 \times 10^{-15} \text{ K}^{-6}$, $m = 0.53$.

The present parameterization can be described as follows. The surface temperature range, over which the albedo changes linearly in the Sellers' parameterization due to a decrease in the presence of ice, is now the same for all latitudes; the lowermost and uppermost temperatures are 210 and 272 K, respectively. The hypothetical contribution of clouds in the albedo-temperature parameterization occurs above this range. A symmetrical "kink" in the albedo-tem-

perature plot centered at 280 K and of triangular shape with a width of 10 K at its base represents this contribution. The albedo at 280 K, the highest point of the triangle, is 0.6. The above described albedo-temperature scheme is illustrated in Fig. 1.

The "kink" in the albedo apparent in Fig. 1 is not prominent in previously available temporally and zonally averaged climatological data on the Earth's cloudiness and radiation budget (Schutz and Gates, 1974). On the other hand, a residual peak near 280 K in seasonally and zonally averaged cloudiness and associated albedo does seem to appear (A. Henderson-Sellers, personal communication, 1981), when carefully analyzing some recent remote-sensing observations (Winston *et al.*, 1979). Clearly the enhanced baroclinic activity discussed by Namias (1964, 1978) and by Goody (1980) is longitude-dependent and its latitudinal position, as well as its location and duration in time, will vary.

Circumstantial evidence for temporal variation of this cloud band can in fact be found in North and Coakley (1979). Analyzing seasonal, zonally averaged insolation, temperature and albedo data, they found near synchronicity between hemispheric albedo and temperature, with both lagging by two-to-three months behind insolation. Their conclusion was that most of the seasonal variation in albedo was not due to a zenith angle effect, but rather to a temperature-profile dominated effect. The cloud band we are discussing could play a major role in this seasonal temperature effect.

Given variability in time and space of the ice-margin related snow track, it is not surprising that it will not show up as a clear peak in averaged statistics (Jacobowitz *et al.*, 1979, Fig. 4). The nonlinear interactions connected with it, however, might give a net effect on climate, even after averaging.

The situation would be similar to the climatology

of blocking (Rex, 1950a,b). The flow patterns of individual blocking events are smeared out by longitudinal and seasonal averaging. Their effect on a season's and a continent's climate are apparent nonetheless. Hence our "kink" is an attempt at parameterizing the climatic effect of cloud-ice margin feedback, even though this feedback itself is barely evident from averaged climate data. The addition of this mildly plausible effect will have interesting consequences for the model's steady-state, as well as time-dependent behavior (Sections 3a and 4b). Its physical basis deserves, therefore, further attention. The ongoing accumulation of climatic satellite data on cloudiness and albedo should provide, within a few years, the verification or invalidation of the mechanism postulated here.

The second change in the temporal structure of the G model is that in Eq. (2a) the albedo of that part of the ground which is covered by ice is assumed not to be determined exclusively by the present temperature $T(t)$, but rather by a weighted linear combination of past temperatures, i.e.,

$$T^*(t) = \int_0^\infty w(s)T(t-s)ds, \quad (6a)$$

with time-dependent weights w . The albedo of a location x with bare ground, i.e., $T(x, t) \geq T_m$, which is not covered by ice at any time of the year (cf. Ghil, 1976), is still determined by the present temperature only. This asymmetric contribution of past temperatures to present albedo was assumed in order to model the slow build-up and rapid melting of ice sheets (e.g., Imbrie and Imbrie, 1979): in our model, advancing ice is retarded by past, warmer temperatures affecting the local radiation balance, while the retreat of ice immediately permits the establishment of a new, more positive radiation balance.

The physical reasoning behind these assumptions is that there is a time lag between the earth's surface temperature and global ice volume (Källén *et al.*, 1979; Ruddiman and McIntyre, 1979). The time scale over which ice in its various manifestations affects the terrestrial climate is very wide (Mitchell, 1976). For large continental ice sheets the times for advance and retreat are both very long and of the order of 10^3 years.

Källén *et al.* (1979) and Ghil and Le Treut (1981) have studied models in which the mass budget of continental ice sheets and their plastic flow are represented explicitly, and coupled to the surface radiation balance. They have shown that in such a coupled system, self-sustained oscillations obtain. These oscillations are characterized by the maximum ice extent lagging about one-quarter period behind the maximum temperature. Such a quarter-phase lag is substantiated by the geochemical work of Ruddiman and McIntyre (1979, 1981) with North Atlantic

deep-sea cores. They suggest 1000–6000 years for the length of the phase lag.

In determining the albedo of the ice-covered ground, the weight assigned to a past temperature $T = T(t-s)$, where $s = 0$ denotes the present temperature, is given by the truncated Gaussian form

$$w(s) = \begin{cases} Ae^{-(\tau-s)^2/2\sigma^2}, & 0 < s < 2\tau \\ 0 & 2\tau < s, \end{cases} \quad (6b)$$

where A is a normalizing constant over the time-lag tail, σ the half-width of the distribution, and τ the value of the time lag at which the maximum of the distribution occurs. We shall denote the albedo computed according to the prescription above by $\alpha = \alpha^*(T^*; \tau, \sigma)$, or simply α^* . When delay effects are ignored, we shall use the notation $\alpha = \alpha(T; 0, 0)$, or simply α .

In the absence of direct observational knowledge on the weights $w(s)$, expression (6b) seemed to be the most reasonable one. Both τ and σ are prescribed parameters of our model. The estimates of τ or σ which could be made from the theoretical work of Källén *et al.* (1979) and from the observational work of Ruddiman and McIntyre (1981) are only approximate. Therefore, various values of τ and σ were used during the actual computation, and effects of changing τ and σ on the solutions were studied. Numerical experiments are made with several values of τ that cover a realistic range of time lags, $O(10^3-10^4)$ years. Shorter values of τ , $O(10^2)$ years, were only used to better understand model behavior, mathematically as well as physically.

This completes the description of the present model. The numerical methods used for the computation of its solutions are described in Appendix A.

3. Stability results

a. Steady-state structure of the model: Internal stability

For present-day insolation conditions, $\mu = 1$, the BG model has five steady-state solutions with positive absolute temperatures. Their computation is described in Appendix A. We denote them, in order of decreasing mean temperature, by $T_1(x)$, $T_2(x)$, \dots , $T_5(x)$. The relevant physically interesting quantities for each of the steady-state solutions are given in Table 3. For comparison, the corresponding quantities for the data climate $\tilde{T}(x)$ are also included.

The original G model, like other Budyko-Sellers models with albedo-feedback only, had three steady-state solutions with positive temperatures. Another model studied by Bhattacharya (1979) and by Ghil and Bhattacharya (1979), using a slightly different albedo-temperature curve, had seven. This shows the dependence of the number of physically possible

TABLE 3. Steady-state solutions of the BG model.* \bar{T} denotes the spatial mean of a solution.

Climate	\bar{T} (K) Steady-state solution	\bar{T} (K) After 5° latitude grid interpolation	\bar{T} (K) Asymptotic	θ_d e -folding time (years)	$T(0)$ (K) Polar temperature	ΔT (K) Equator-to-pole temperature difference
\bar{T}	287.20				247.36	51.99
T_1	286.61	287.07	285.42	-2060	257.59	39.60
T_2	281.67	282.13	283.63	+520	254.18	38.12
T_3	272.94	273.14	273.14	-35	249.79	27.74
T_4	241.96	242.14	244.13	+230	216.77	33.92
T_5	175.17	175.26	208.88	-210	169.18	7.89

* See Appendix A for further details on the difference between various ways of computing the steady states. Negative e -folding times, or relaxation times, indicate stability; plus signs indicate instability or growth of small perturbations. Compare also with Table 3 of Ghil (1976) for results with the G model.

model steady states on the exact shape of the albedo-temperature dependence. Notice that the number and shape of steady states does not depend on either the heat capacity $C(x)$ or the time lag [Eq. (6)] in the albedo.

Solution $T_1(x)$ of this model corresponds roughly to the present climate, and to the uppermost "climate" of the G model, while $T_5(x)$ corresponds to the "deep-freeze" of the G model. In order to understand better the roles of $T_2(x)$, $T_3(x)$ and $T_4(x)$, we have to consider the solutions' stability.

Internal stability of the steady states in Table 3, in the absence of delay effects, was investigated by carrying out time integrations of Eq. (4) with $\alpha = \alpha(T; 0, 0)$ and with initial conditions (5c) close to each steady state. The numerical method for carrying out these integrations is described in Appendix A. Time-dependent solutions of such an initial-value problem will converge in time to the steady state nearby if it is stable, and diverge from it if the steady state is unstable. The corresponding relaxation times, or exponential decay times, are also given in Table 3 for the stable states. For the unstable ones, the exponential, or e -folding, growth times are given.

The results indicate that $T_1(x)$, $T_3(x)$ and $T_5(x)$ are internally stable, while $T_2(x)$ and $T_4(x)$ are unstable. Hence, $T_3(x)$ is another stable steady state in the BG model, not present in the G model or other Budyko-Sellers models. It is introduced by the "kink" in the albedo-temperature curve. To convince us further of this fact, we next consider the dependence of the steady-state structure on the insolation parameter μ , the fractional change in the "solar constant."

The average temperature \bar{T} of the model steady states is plotted in Fig. 2 against μ over a range $0.5 \leq \mu \leq 2.3$. The graph $\bar{T} = \bar{T}(\mu)$ resembles a double S. The ascending branches (A, C and E) intersect the vertical line $\mu = 1$ at \bar{T}_1 , \bar{T}_3 and \bar{T}_5 , respectively. They are separated by the descending branches B and D, which contain the points $(1, \bar{T}_2)$ and $(1, \bar{T}_4)$, respectively. The connection between the slope of a branch and the internal stability of the steady states

on that branch is the same for this model as conjectured by Budyko (1972) and proven rigorously for a class of simple models by Cahalan and North (1979). The positive slope of the branch, $d\bar{T}/d\mu > 0$, implies that the steady states along that branch are internally stable, while negative slope implies that they are unstable.

Comparing our Fig. 2 with Fig. 6 of Ghil (1981a), which gives the S-shaped steady-state structure of

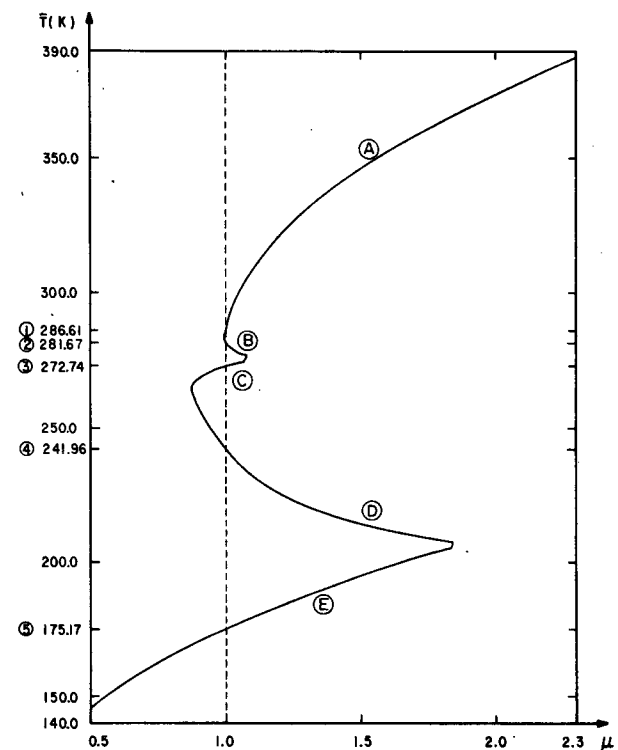


FIG. 2. Bifurcation curve, $\bar{T} = \bar{T}(\mu)$, for the steady-state structure of the model: \bar{T} is globally and annually averaged surface temperature and μ is fractional change in insolation. At present insolation conditions, $\mu = 1$, there are five climates (see Table 2 for details). The branches through climates 1-5 are denoted by A-E. The appearance of the branches B and C is due to the "kink" in the albedo (Fig. 1).

the G model, it becomes clear that $T_4(x)$ of the BG model, and its branch D correspond roughly to the intermediate, unstable steady state of the G model, and to its branch B. The slight distortion of branches A and D of the BG model, near $\mu = 1$, and the presence of the additional branches B and C of this model, is due to the albedo kink at $T = 280$ K (Fig. 2). In particular, the "sensitivity" of the "present-climate" branch A to changes in μ is enhanced by the postulated cloud-albedo feedback mechanism.

For a zero-dimensional (0-D) globally-averaged model, the number of steady states equals the number of intersections of the $R_i = R_i(\bar{T})$ curve with the $R_o = R_o(\bar{T})$ curve (Crafoord and Källén, 1978, Fig. 1; Ghil, 1981a, Fig. 4). There would be three intersections for a 0-D version of the G model, and five intersections of a 0-D version of our present model. For a one-dimensional (1-D) model, things can be slightly more complicated (Ghil and Bhattacharya, 1979; Ghil, 1981a). The existence of the two additional branches, B and C, in the present model, and the close correspondence between its branches, A, D and E, and the three branches of the G model is therefore of some interest.

In particular, values of \bar{T} on the two stable branches A and C, for μ close to 1, are within O(10 K) of each other. This can make the model interesting in studying glaciation cycles: a C-state could represent a glacial climate, while an A-state could be interglacial. Indeed, the difference in temperature between the last glacial temperature minimum, and the present interglacial temperature near-maximum is currently believed to be of the order of magnitude of a few degrees, although opinions on its exact size vary.

To establish a possible connection between our model and the glaciation-cycle problem, we have to consider next the model's time-dependent behavior. In the absence of delay effects, this behavior is rather simple. We shall discuss it first, and consider the effects of introducing delays afterwards.

b. Variational principle: Structural stability

For fixed μ , $\mu = 1$ say, we have seen in the previous subsection that initial states close to a steady state will evolve toward that steady state if it is internally stable, and away from it if it is unstable. In more precise language, this type of internal stability is *linear* stability: it applies only *very* close to a steady state. To find out what happens further away from the steady states, and, even more ambitiously, for any initial state, one has to consider *nonlinear* stability. This can be easily done for the problem at hand due to the existence of a *variational principle*.

We consider the functional (Ghil, 1976)

$$J\{T(x); \mu\} = \int_0^1 \{ \frac{1}{2} p(x) T_x^2 - r(x) G(x, T(x); \mu) \} dx, \quad (7a)$$

with $p(x)$, $r(x)$ and $G(x, T)$ being related to the coefficients of Eq. (1) by

$$p(x) = (2/\pi)^2 \sin(\pi x/2) \cdot k(x), \quad (7b)$$

$$r(x) = \sin(\pi x/2), \quad (7c)$$

$$G(x, T; \mu) = \int_0^T [R_i(x, S; \mu) - R_o(x, S)] dS. \quad (7d)$$

Here

$$\int_0^T F(x, S) dS$$

is the indefinite integral of $F(x, S)$ at fixed x with respect to the variable S . For instance, if $F(x, T) = R_i(x, T) - R_o(x, T)$ were given by $F = ax + bT(x)$, then G would be

$$G = axT(x) + \frac{1}{2} bT^2(x).$$

Notice also that the parameter μ , which appears only as a coefficient in $R_i(x, T(x); \mu)$ [cf. Eq. (1b)] does not play any role in the integration.

The steady-state form, $\partial T/\partial t = 0$, of Eq. (4) is the *Euler equation* (Courant and Hilbert, 1953, Chap. 4) of the functional $J\{T; \mu\}$. Such a variational formulation of equations governing simple climate models was also considered by North *et al.* (1979). It was recently applied to the study of stochastic perturbations for such simple climate models by Nicolis and Nicolis (1981), Nicolis (1982) and Sutera and collaborators (Sutera, 1981; Benzi *et al.*, 1982).

We shall describe first the functional $J\{T(x); \mu\}$ for a fixed value of μ , $\mu = 1$, say. Then, given any temperature profile $T = T(x)$, Eq. (7) assigns to it a certain real number J . For visualization purposes, let $\{\phi_n(x)\}$ be a set of basis functions for the temperature profiles, so that any profile $T(x)$ can be written as

$$T(x) = \sum_1^\infty T_n \phi_n(x).$$

Such a set of basis functions can be found for this problem, since it is a generalized Sturm-Liouville problem (Ghil, 1976). It was shown by North *et al.* (1979) that it is convenient to let the Legendre polynomials, with $\cos(\pi x/2)$ as argument, be the basis functions.

Using the coefficients T_n as coordinate axes, it is possible to plot $J\{\sum T_n \phi_n(x); 1\}$ as the "height" h of the hyper-surface given by Eq. (7), $h = J\{T\}$. For a truncated representation of $T(x)$, with $n = 0, 2$ only, such a contour plot appears in North *et al.* (1979, Fig. 2).

In a plot of $J\{T(x); 1\}$, stable steady states of Eq. (4) appear as *minima*, while unstable ones will appear normally as *saddle points*, i.e., points in the neighborhood of which the surface rises in certain directions, but descends in at least one direction. The evolution of a solution of Eq. (4), again with no delays, $\alpha = \alpha(T; 0, 0)$, can be pictured as motion along the surface $h = J\{T; 1\}$, i.e.,

$$\tau(x)C(x)T_t = -\delta J\{T; 1\}/\delta T; \quad (8)$$

here $\delta J/\delta T$ represents the functional derivative of J with respect to the temperature profiles $T(x)$. If the basis $\{\phi_n(x)\}$ is orthonormal and $C(x) = \text{constant}$, then Eq. (8) can be rewritten (North *et al.*, 1979) as a decoupled system of ordinary differential equations for the evolution of the coefficients $T_n = T_n(t)$:

$$CT_n = -\delta J/\delta T_n.$$

Here a dot denotes the time derivative.

It follows from (8) that the solutions of (4) will always "flow" downslope. It can also be shown that the surface $h = J(T)$ tends to infinity far away from the steady-state solutions. Hence the "flowpath" or trajectory from any initial state will eventually end up at one of the minima. A trajectory could be slowed down, however, near saddle points, and leave their neighborhood only after a relatively long time (Ghil, 1976; Ghil and Bhattacharya, 1979).

This discussion elucidates the model solutions' nonlinear stability, for fixed μ ($\mu = 1$) and in the absence of delay effects, $\alpha = \alpha(T; 0, 0)$. The surface $h = J\{T; 1\}$ has three minima, at $T = T_1(x)$, $T_3(x)$, $T_5(x)$. These are surrounded by "cauldrons," or *attractor basins*. The basins are separated by ridges; at the lowest points of the ridges sit the saddle points, or "passes," $T = T_2(x)$, $T_4(x)$. This whole structure of three basins and two ridges is itself at the center of a larger cauldron, with h rising to infinity all around. Thus the only question for any trajectory, starting at an arbitrary point $[T = T(x), h = J\{T(x)\}]$ on the surface, is: at which one of the three minima will it end?

The study of the model's *structural stability* deals with the way in which this picture changes as the insolation parameter μ changes. From Fig. 2 it is clear that, as μ decreases from $\mu = 1$, the bottom $T_A(x; \mu)$ of the cauldron originally at $T_1(x)$ rises and eventually coalesces, at $\mu = \mu_2 = 0.999$, with the pass $T_B(x; \mu)$ originally at $T_2(x)$. Finally, this whole part of the "topography" merges into a slope which descends into the cauldron with bottom at $T_C(x; \mu)$. As μ decreases further, it is the turn of the cauldron C to be flattened out of existence, leading to the disappearance of pass D as well, at $\mu = \mu_1 = 0.88$. Thus, for small μ , only the cauldron E is left. All the while, the topography still rises to infinity in the distance.

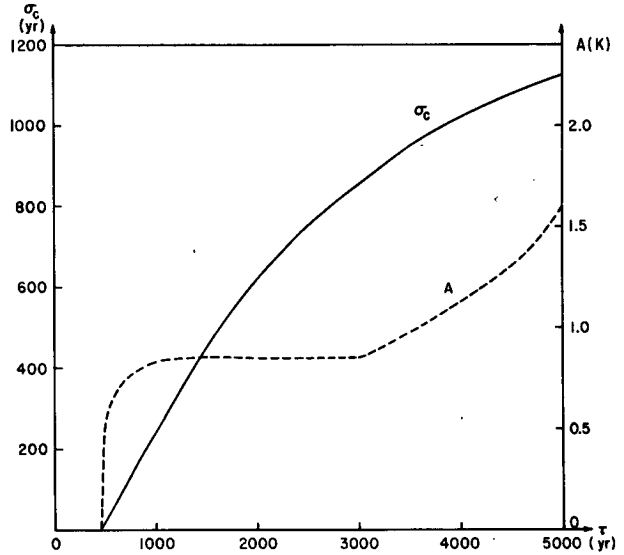


FIG. 3. Dependence of small-amplitude model oscillations on the lag parameters τ and σ : τ is the mean value of the lag, σ is its half-width. The solid curve (scaled by the axis to the left) shows the value of σ_c which separates the sustained oscillation regime, for smaller σ , from the stable steady state regime, for larger σ . The dashed curve (scaled on the right) shows the peak-to-peak amplitude A of the sustained oscillations, as a function of τ ; the dependence of A on σ , for $\sigma < \sigma_c$, is very weak. Notice the plateau in $A = A(\tau)$ for $1000 \leq \tau \leq 3000$ years.

As μ increases, it is cauldron C which disappears first, together with pass B, at $\mu = \mu_3 = 1.075$. Then cauldron E and pass D disappear, at $\mu = \mu_4 = 1.844$, leaving only cauldron A for large μ . Thus the model's internal stability, nonlinear as well as linear, varies smoothly with the external parameter μ . Only a number of jumps occur, at four values of μ , when the number of steady-state solutions changes in pairs, from one to three to five, and then back to three and to one, as μ increases from 0.5 to 2.5. An existing steady state does not change its internal stability as μ varies.

4. Time-dependent model behavior: delay effects

Up to this point we have investigated the model's steady-state solutions and, in the absence of delay effects, its time-dependent solutions. The latter could be represented by trajectories flowing downslope along the surface $h = J\{T(x); \mu\}$ given by Eq. (7), toward the existing minima. The number of minima corresponding to positive temperature profiles, one, two or three, depends on the value of μ .

a. Importance of delay effects

We are ready to study now the effect of delays as introduced in Eq. (6), $\alpha = \alpha^*(T^*; \tau, \sigma)$. In this subsection, some basic concepts on delay effects and

their connection to the variational principle of Section 3b are introduced. The reader, impatient to see the main results of this investigation, can proceed directly to Section 4b, and refer back to 4a as needed.

That delays can drastically alter time-dependent behavior is easily seen from the following simple, linear example (Driver, 1977, Sec. 22):

$$\dot{u}(t) = -u(t - \tau). \quad (9)$$

In the absence of time delays [$\tau = 0$] Eq. (9) has the single stable steady state $u = 0$, and all solutions tend exponentially to it, i.e.,

$$u(t) = u_0 e^{-t}.$$

With a time delay $\tau = \pi/2$, however, Eq. (9) has the family of nontrivial, periodic solutions

$$u(t) = u_0 \cos t + v_0 \sin t, \quad (10)$$

where u_0 and v_0 are arbitrary. It can be shown that these solutions are stable in a suitable sense with respect to changes in the initial data of (9) (Hale, 1977, Chap. 1).

The same solutions (10) would obtain if one considered, instead of (9), the system of two equations with *no* delays,

$$\dot{u} = v, \quad (11a)$$

$$\dot{v} = -u, \quad (11b)$$

and with initial conditions

$$u(0) = u_0, \quad v(0) = v_0. \quad (11c)$$

The obvious identification to be made in connecting the two points of view is

$$v(t) = -u(t - \pi/2). \quad (11d)$$

The *delay differential equation* (DDE) (9) is thus equivalent, in a sense, to a system of two ordinary differential equations (ODE's), Eqs. (11a,b). In this interpretation, the lagged variable v acquires a certain independence from u , the two being coupled by the system (11).

The steady-state form of Eq. (9) is the Euler equation of the functional

$$J\{u\} = u^2/2.$$

In this trivial case, J is just a usual real-valued function of the scalar u . Eq. (9), with *no* time delay ($\tau = 0$) can be written in terms of J as

$$\dot{u} = -dJ/du. \quad (12)$$

Clearly, (12) represents flow downslope on the surface $h = u^2/2$; in this simple example, the "surface" is just a concave curve in the (u, h) plane.

We would like to interpret the solution with no delay as a point rolling down the surface $h = J\{u\}$. A little care has to be exercised in this interpretation,

and in viewing $J\{u\}$ here, or $J\{T(x); u\}$ in Section 3b, as a *potential*. Namely, in such an interpretation, u would have to be the *velocity*, rather than the position of a particle, in the force field $-dJ/du$. Then Eq. (12) can be viewed as the equation of motion of a particle with "zero mass," and velocity u . Since it has no inertia, the particle stays at the bottom of the cauldron, where forces are zero, once it reaches it.

Actually, Eq. (9) is a first-order ODE for $u(t)$, rather than a second-order ODE; it contains *only* the "velocity" u , rather than containing the "position" of the particle as well. Similarly, Eq. (4) is a parabolic PDE, containing only the first time derivative of $T(x, t)$. It does not contain the second time derivative, as a hyperbolic PDE, or wave equation, would.

The fact that only first-time derivatives are present in (4) or (9) avoids the contradiction which would otherwise arise from J depending on velocity, and hence on the particular *trajectory* of a "particle," rather than on position only. The contradiction is removed by the "position" of the particle being absent from the equation altogether. Keeping this in mind, the geometric interpretation of Eqs. (8) and (12) is still very helpful for understanding the results in the present and preceding sections. The word "flow" we used in Section 3b is entirely correct in this interpretation for a fluid moving only under the effect of viscous forces from an arbitrary initial position to the bottom of the cauldrons. Thus $J\{u\}$ in this case corresponds roughly to a velocity potential, in the sense of fluid mechanics.

We wish now to explain intuitively why the solution of Eq. (9) with time delay $\tau = \pi/2$ does not stay put at the bottom of the cauldron ($u = 0$, $h = 0$), but oscillates around it with amplitude $(u_0^2 + v_0^2)^{1/2}$, given by its initial values. The foregoing discussion of the case with no delay gives the desired clue.

Let us interpret u as position, $v = -u(t - \pi/2)$ as velocity, and write the equation governing the motion as

$$\ddot{u} = -u, \quad (13a)$$

with initial conditions

$$u(0) = u_0, \quad \dot{u}(0) = v_0. \quad (13b,c)$$

The solution is still (10), and this is but another way of viewing (9) or (11).

Eq. (13a), however, has a variational principle. It is the *Lagrange equation* (Goldstein, 1980, Sec. 1.4)

$$\frac{d}{dt} \frac{\partial \mathcal{L}}{\partial \dot{u}} - \frac{\partial \mathcal{L}}{\partial u} = 0, \quad (14a)$$

for the Lagrangian

$$\mathcal{L} = (\dot{u}^2 - u^2)/2, \quad (14b)$$

where \mathcal{L} is the difference of the kinetic energy \mathcal{T}

and the potential energy \mathcal{V} , i.e.,

$$\mathcal{L} = \mathcal{T} - \mathcal{V},$$

$$\mathcal{T} = \dot{u}^2/2, \quad \mathcal{V} = u^2/2.$$

In this interpretation, $\mathcal{V} = J\{u\}$ becomes a potential, with the force equal to $-d\mathcal{V}/du$, in the usual sense of particle mechanics. The variational principle is simply Hamilton's principle (Goldstein, 1980, Sec. 2.3).

The particle whose motion is governed by Eq. (13) is now endowed with unit mass, and it does not come to rest at the bottom of the potential well $h \equiv \mathcal{V} = u^2/2$. It continues rather to oscillate indefinitely, since friction is absent, with amplitude $(u_0^2 + v_0^2)^{1/2}$, so as to conserve its total energy

$$\mathcal{E} = \mathcal{T} + \mathcal{V} = (\dot{u}^2 + u^2)/2.$$

We see from both (11) and (13) that the effect of delays is to introduce an *inertia* into a first-order equation and to allow therefore the possibility of oscillations where none could obtain in the absence of delays.

We can think of Eq. (9) as the local linearization, around one solution of the steady-state form of the equation, of a nonlinear DDE. For a nonlinear DDE, one would expect periodic solutions, if they exist at all, to be present for a whole range of delay values close to $\pi/2$ and, for each value of τ , to be unique and stable (Hale, 1977, Chap. 10). Such behavior was indeed observed for a version of our model in which the delays are localized in time ($\sigma = 0$), i.e., $w(s)$ in (6a) is a δ -function (Ghil and Bhattacharya, 1979, Fig. 7 and Table 1). In fact, in this discrete-delay version of our model, the branch of stable, periodic solutions seemed to bifurcate from a stable steady state by Hopf bifurcation (Hale, 1977, Chap. 11).

In the following we shall discuss results with the present, distributed-delay version of the model, which is presumably somewhat more realistic. Solutions will show behavior which is more complex than simply-periodic. The preceding discussion of the simple DDE (9) and of its variational interpretation (14) will help in the heuristic explanation of solution behavior for the BG model.

Further useful references on DDE's and the differences in solution behavior between them and ODE's are Hale (1971, Chap. 1) and MacDonald (1978).

b. Model results

This subsection contains the main results of our investigation. It shows that the simple model with delayed albedo described in Section 2 can exhibit quasi-periodic, as well as nonperiodic behavior. The spectral analysis of the model's solutions in time

shows a continuous power background, with discrete peaks superimposed on it.

1) DEPENDENCE OF OSCILLATIONS ON LAG PARAMETERS

We were mainly interested in model oscillations near the data climate, i.e., the actual climate of the present. Hence, initial conditions near model climates 1 and 3 were used, and present insolation conditions, $\mu = 1$, were applied.

Temperature and albedo data for the beginning of the numerical time-dependent computations were taken to correspond to each other, i.e., $\alpha = \alpha(T; 0, 0)$ for $0 \leq t < 2\tau$, as described in Appendix A. At $t = 2\tau$, the effect of the delays is allowed to begin, $\alpha = \alpha^*(T; \tau, \sigma)$, and it is kept for the rest of the calculation.

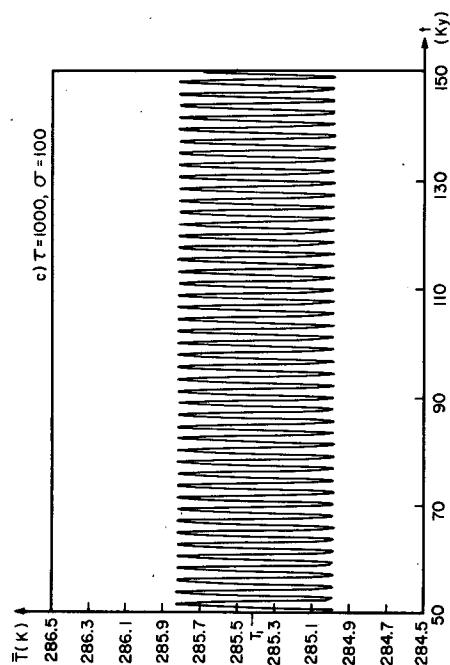
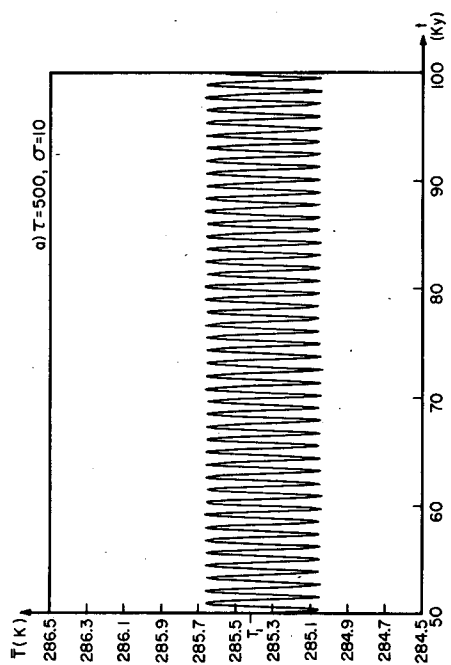
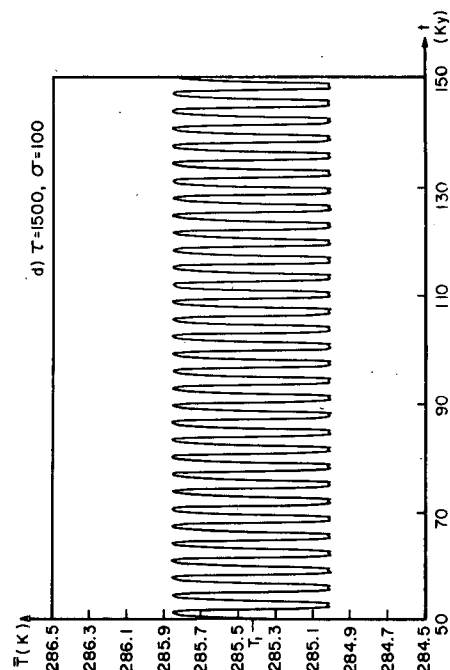
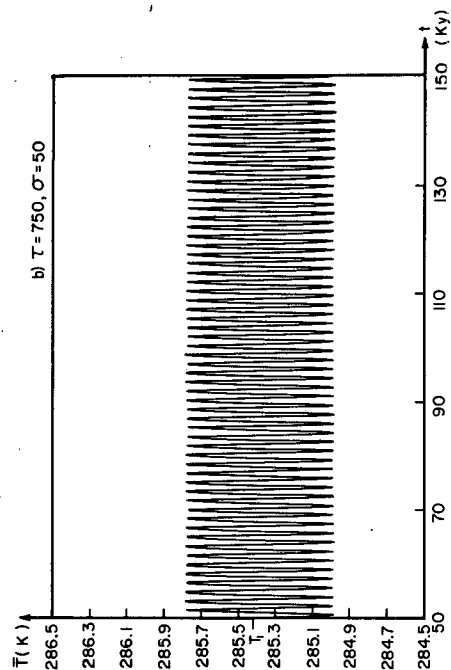
No oscillations obtain when temperatures are equal to or higher than at present, $T(x, 0) \geq T_1(x)$. In other words, the uppermost model climate is not destabilized by delay effects as long as temperatures stay as warm or warmer as they are at present.

For large negative perturbations, $T_1(x) - 10 \text{ K} < T(x, 0) \leq T_1(x) - 7.5 \text{ K}$, the presence and nature of oscillations depends on the value of the lag parameters τ and σ . Recall that [cf. Eq. (6)] τ gives approximately the mean value of the distributed lag, while σ gives its half-width, i.e., the extent to which the Gaussian weight $w(s)$ of (6b) differs from a δ -function. The connection between DDE's with distributed delays and their simpler, discrete delay ($\sigma = 0$) counterparts is discussed in MacDonald (1978, Chap. 4).

For a given τ , there exists a critical value of σ , $\sigma_c = \sigma_c(\tau)$, such that for $\sigma > \sigma_c$ there are no sustained oscillations. In other words, if the influence of the past temperature history is nearly averaged over an entire cycle, incipient oscillations are damped out. The values of σ_c as a function of τ are given in Fig. 3.

For $\sigma \leq \sigma_c$, oscillations about climate 1 obtain. Their amplitude depends mostly on τ , and very little on σ . The peak-to-peak amplitude A of the oscillations in mean temperature [$\bar{T} = \bar{T}(t)$] as a function of τ is also shown in Fig. 3. The shape of the curve $A = A(\tau)$ is interesting. The amplitude first increases sharply with τ from $\tau = \tau_0 \approx 475$ years to $\tau \approx 1000$ years, then stays nearly constant between $\tau \approx 1000$ and 3000 years, to increase again up to $\tau = 10\,000$ years. It is zero for $\tau < \tau_0$; over the constant range, it is $\sim 1 \text{ K}$. The temporal average of the oscillations in \bar{T} is independent of τ ; it equals precisely $\bar{T}_1 = 285.4 \text{ K}$.

The actual shape of the oscillations in the spatially averaged temperature $\bar{T} = \bar{T}(t)$ is shown in Figs. 4a-4f. For the lower values of τ , $500 \text{ years} \leq \tau \leq 1000$ years, a predominant oscillation with a period ap-



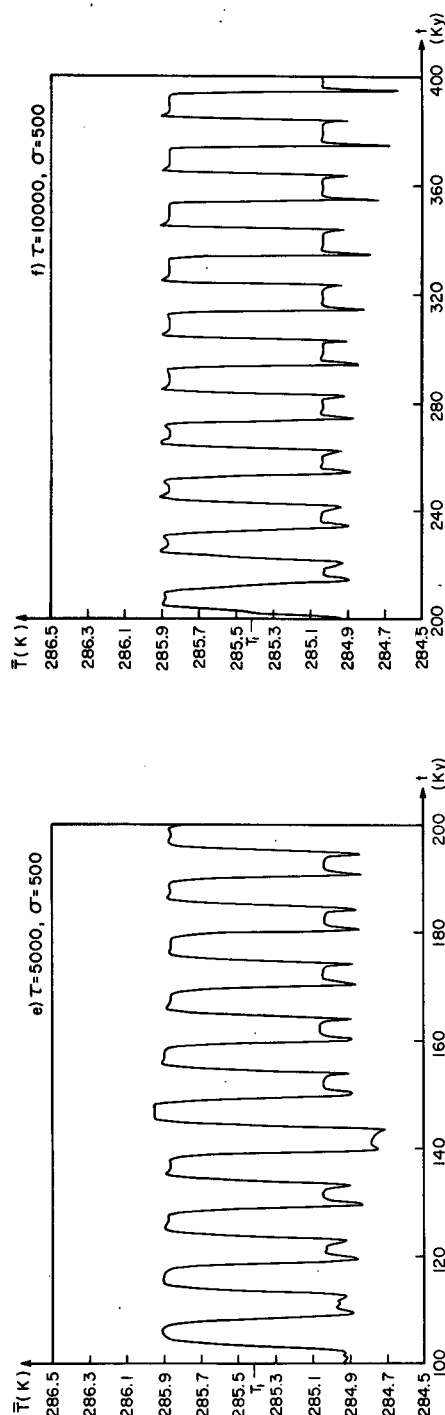


FIG. 4. Time evolution of the globally averaged temperature $\bar{T} = \bar{T}(t)$. Sustained oscillations around model climate 1 occur. The values of the lag parameters (τ, σ) are marked in Figs. 4a–4f. Time units are 1 Ky = 1000 years. For plotting purposes, a running mean (moving average) over 100 years of model solutions was used. The numerical output itself, as well as running means taken over other interval lengths, did not exhibit any behavior different from that shown here. Notice the change in character of the oscillations from roughly sinusoidal waves to square waves, with irregular spikes, at about $\tau = 1500$ years (Fig. 4d).

proximately equal to 2τ is evident (Figs. 4a–4c). This “carrier wave” shows a slight amplitude modulation with periods of the order of 10 – 100τ . Both the carrier wave and the modulations appear to be nearly sinusoidal.

At $\tau \approx 1500$ years (Fig. 4d), the nature of the oscillations seems to change. For $\tau = 5000$ and $10\,000$ years (Figs. 4e, 4f), the shape of the “carrier wave” becomes square, rather than sinusoidal. Spikes of irregular shape, height and spacing protrude from the basic square wave.

2) STABILITY OF OSCILLATIONS

We studied the stability of both types of oscillation, the approximately sinusoidal as well as the irregular ones, to perturbations. The perturbations were applied at $t = t_1 = 50\,000$ years, when the oscillations are already well established. First, uniform perturbations were introduced, $T'(x, t_1) = T(x, t_1) + T_0$, $T(x, t_1)$ being the unperturbed solution at time $t = t_1$, and T_0 the constant perturbation.

“Warm” perturbations, $T_0 \geq -7.5$ K, had the effect of damping out the oscillations. The oscillations were stable to “cold” perturbations, -10 K $\leq T_0 \leq -7.5$ K: after a transient response period, the same type of asymptotic behavior occurred as for the unperturbed solution. The response to both warm and cold perturbations agrees with the results on initial data $T(x, 0)$, viz., existence or nonexistence of sustained oscillations, respectively.

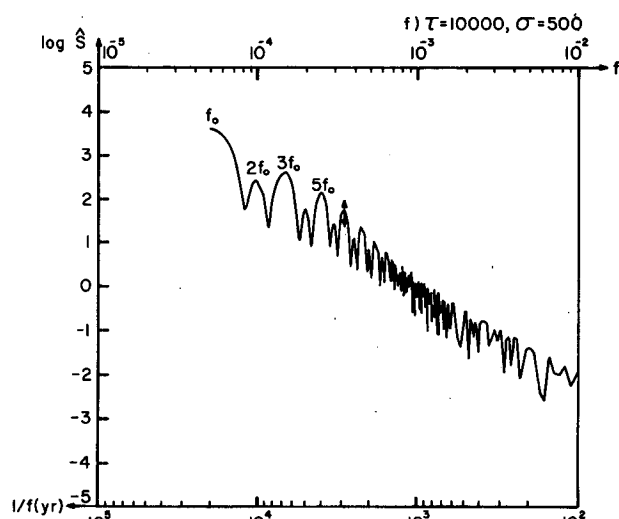
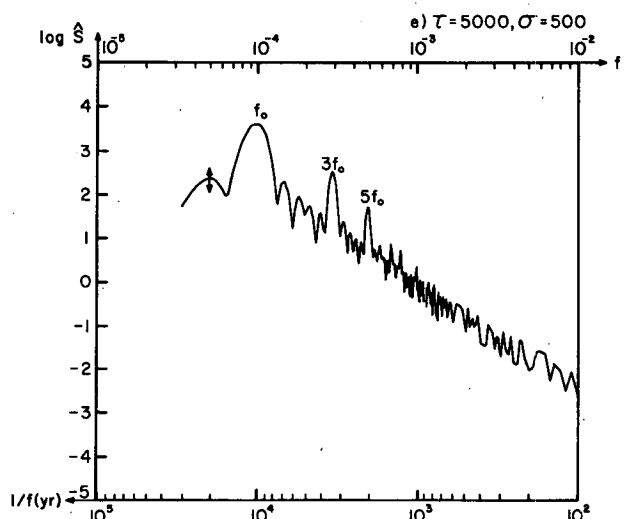
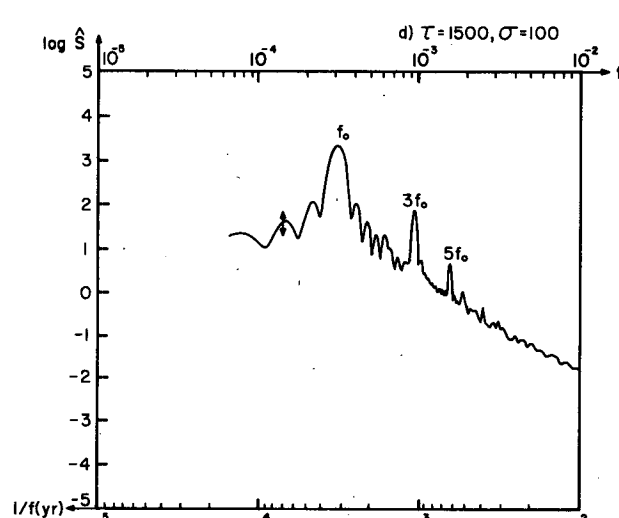
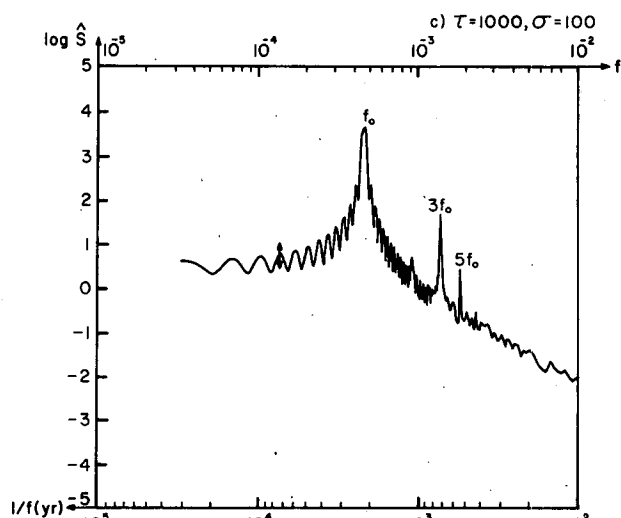
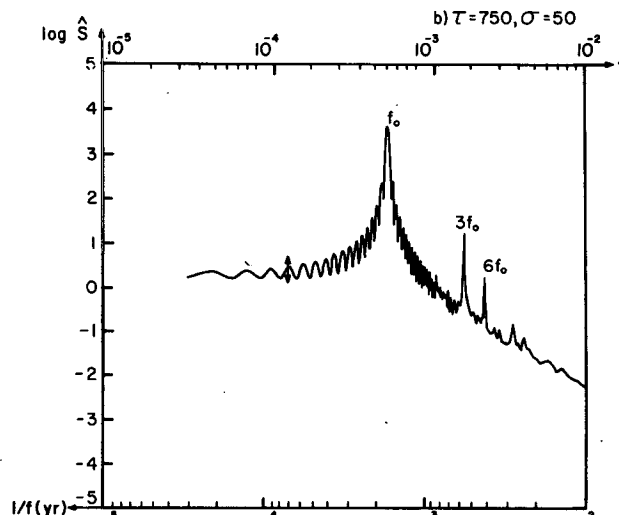
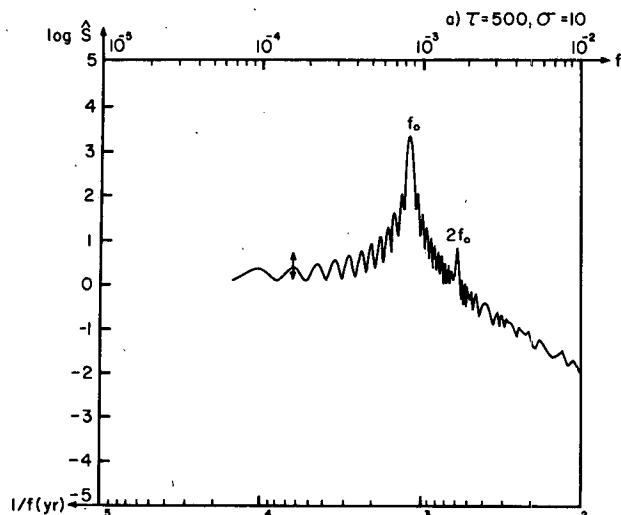
When nonuniform, random perturbations, $T'(x, t) = T(x, t_1) + \theta(x)$ were applied, with θ random, either stability or damping obtained, according to the mean value and the standard deviation of θ . The reasons for this will be discussed later, along with the geometric interpretation of the oscillations.

3) TRANSITION TO IRREGULAR BEHAVIOR

In order to understand better the nature of the oscillation for given, fixed τ , as well as its change with τ , we performed a spectral analysis of the solutions obtained. A spectral analysis package written by D. L. Vulis and I. L. Vulis was used; the package had been previously tested and it was implemented in Vulis and Monin (1979). For the sake of completeness, the analysis method used is described in Appendix B. The estimated spectra $\hat{S}(f)$ of the solutions in Fig. 4 are shown in Fig. 5 on a log-log scale, f being the frequency.

In Figs. 5a–5c a very strong peak at a frequency f_0 given by $f_0 \approx 1/(2\tau)$ dominates the spectrum. At its right appears a number of almost equally high, but narrower peaks, the *harmonics* of the basic oscillation. The small-amplitude, broad undulations in the spectrum to the left of f_0 do not represent significant peaks.

The three most significant spectral peaks for each



value of τ in Figs. 4a–4f and 5a–5f are given in Table 4. The second significant peak corresponds to $2f_0$ in Fig. 5a, and to $3f_0$ in Figs. 5b–5f. A third significant peak is absent in Fig. 5a; it is located at $6f_0$ in 5b, at $4f_0$ in 5c, and at $5f_0$ in Figs. 5d–5f.

Starting with Fig. 5c, the number of narrow peaks superimposed on the continuous part of the spectrum increases. The width of these peaks increases in Fig. 5d. In Fig. 5e the distinction between peaks and background decreases further, to disappear almost entirely in Fig. 5f.

The change in the character of the oscillations (Fig. 4d) and of their spectrum (Fig. 5d) for $\tau \approx 1500$ years corresponds to a transition from quasi-periodic to nonperiodic, irregular, chaotic behavior. In many fluid flows, such a transition occurs when turbulence sets in. It is currently believed (Ruelle, 1980) that the transition in the physical system's behavior can be described by the change in nature of the attractor set for the mathematical model of the system.

The attractor set of a dynamical system whose asymptotic behavior is stationary contains only isolated stable points. If asymptotic behavior of the system's solutions is periodic or quasi-periodic, the attractor set contains stable limit cycles (periodic) and stable multi-dimensional tori (quasi-periodic). Non-periodic behavior (Lorenz, 1963) is associated with the presence of a "strange attractor."

A stable equilibrium point is itself zero-dimensional and it is attracting in every possible direction of the system's phase space. Stable limit cycles and tori are one-dimensional or n -dimensional, respectively, with $2 \leq n < d$, d being the dimension of the phase space, i.e., the number of the system's degrees of freedom. They are attracting in all directions "perpendicular" to their "surface," viz., in $d - n$ independent directions; they are *neutrally* stable in all directions which are "parallel" to their surface, viz., in n orthogonal directions.

Strange attractors can occur in continuous-time dynamical systems (e.g., systems of ODE's) only for $d \geq 3$. They are also attracting in $d - n$ independent directions, like the attractor sets for asymptotically (quasi-) periodic solutions. Their strangeness derives from the fact that they are highly *unstable* in the n directions in their own "surface." Thus trajectories starting anywhere in phase space fall onto the attractor. Afterward, however, they are repulsed from any point on the attractor they are close to, and therefore from each other. This leads to a perpetual irregular wandering within the attractor set.

TABLE 4. Spectral peaks for model solutions obtained with different lag parameter values (compare Figs. 4 and 5).*

τ (years)	Period of main peak (years)	Period of second peak (years)	Period of third peak (years)
500	1170 (f_0)	590 ($2f_0$)	—
750	1690 (f_0)	560 ($3f_0$)	280 ($6f_0$)
1000	2200 (f_0)	730 ($3f_0$)	550 ($4f_0$)
1500	3200 (f_0)	1060 ($3f_0$)	640 ($5f_0$)
5000	10 240 (f_0)	3420 ($3f_0$)	2050 ($5f_0$)
10 000	20 000 (f_0)	6800 ($3f_0$)	4060 ($5f_0$)

* The peaks, in order of height above the continuous background, are determined from the spectral density function, using various filter parameter values (see Appendix B for details). They are very stable to changes in these values. Next to each peak, the dominant (f_0) or approximate harmonic (kf_0) is marked.

Rising of the background noise around pre-existent spectral peaks is typical of the apparition of a strange attractor in a dynamical system (Ruelle, 1980) and of the onset of turbulence in a fluid (Golub and Benson, 1980; Libchaber and Maurer, 1980). We conjecture, therefore, that our climate model equations (4)–(6) exhibit a strange attractor. A strange attractor for a relatively simple ODE with a discrete delay was studied recently in great detail by Farmer (1982). The changes in their solution's spectra (*ibid.*, Fig. 3) with τ are very similar to ours.

The almost pure red-noise spectrum, with a log-log slope of (-2) , to the right of f_0 in Fig. 5f is typical of well-developed turbulence. It is interesting to notice, however, that the time evolution of the corresponding solutions (Figs. 4e, 4f) is relatively smooth in shape, with the size and location of the spikes only being irregular. This might point to a geometric structure and stability properties of the strange attractor somewhat different from those previously studied.

4) LARGE-AMPLITUDE, IRREGULAR BEHAVIOR

So far only those solutions were discussed for which the associated trajectories lay entirely within the cauldron of the potential (7) whose minimum is at $T = T_1(x)$. We turn now to a discussion of other types of behavior for solutions originating in the cauldron around climate 3.

The initial data segment in this case for $0 \leq t < 2\tau$ was $T(x, t) = T_3(x)$, $\alpha = \alpha(T_3; 0, 0)$. For $t \geq 2\tau$, delay effects were introduced by letting $\alpha = \alpha^*(T^*; \tau, \sigma)$. Depending on the values of τ and

FIG. 5. Power spectra of the time series in Fig. 4. Both axes are logarithmic, with the abscissa marked for convenience, at the bottom, in the periods corresponding to the given frequency at the top. Figs. 5a–5f are each the spectrum of Figs. 4a–4f. The dominant peak in each figure is $f_0 = f_0(\tau, \sigma) \approx 1/(2\tau)$. The additional peaks to the right of f_0 are its harmonics kf_0 . A change in the character of the spectrum appears in Fig. 5d; this change is typical of transition from quasi-periodic to non-periodic oscillations. In Fig. 5f, the general slope of the spectrum to the right of the dominant peak is -2 . Units for f are cycles per year.

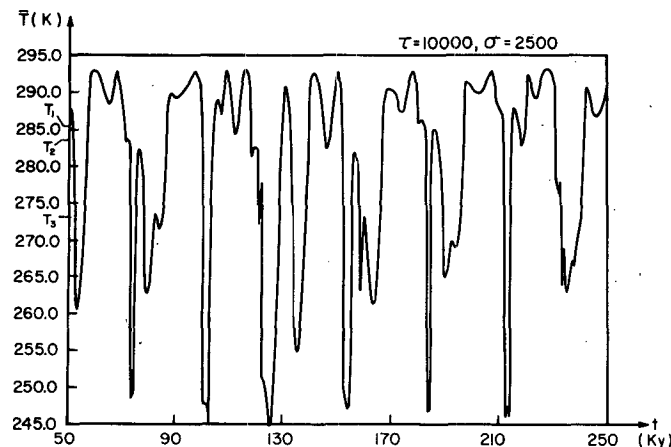


FIG. 6. Large-amplitude oscillation in $\bar{T}(t)$ between the neighborhood of climate 1 and climate 3. The oscillations are very irregular in character; the system shows a tendency to spend more time near its "warm" climate 1, but short excursions to very "cold" temperatures, well below climate 3, are also possible.

σ , oscillations obtain around climate 1, climate 3, or between both.

For $\tau > \tau_0$ and small values of σ , $\sigma < \sigma_1(\tau)$ the solution jumps from the cauldron around $T_3(x)$ to that of $T_1(x)$, and executes a sustained oscillation around $T_1(x)$, as described above (Fig. 4). As σ is increased beyond $\sigma_1(\tau)$, solutions starting at $T_3(x)$ tend asymptotically to $T_1(x)$, as was the case before whenever $\sigma \geq \sigma_c(\tau)$. The new feature here is that, for τ large enough, $\tau > \tau_1$, and for $\sigma > \sigma_2(\tau)$, the solutions exhibit large-amplitude, very irregular oscillations in which they alternate between the two cauldrons (Fig. 6). This behavior prevails for a wide range of σ , $\sigma_2 < \sigma < \sigma_3(\tau)$. For σ still larger and sufficiently large τ , there is a further possible type of behavior, with solutions oscillating around $T_3(x)$ with very small amplitude, $A = O(0.1 \text{ K})$. The values of σ_1 , σ_2 and σ_3 are given in Table 5, for three values of τ .

All these types of behavior are stable for pertur-

TABLE 5. Threshold values of σ for which model solutions starting near climate 3 change character.*

τ (years)	σ_1 (years)	σ_2 (years)	σ_3 (years)
500	40	—	—
1000	200	675	1400
1500	625	625	2100

* For $0 < \sigma < \sigma_1(\tau)$, small-amplitude oscillations [$O(1 \text{ K})$] around $T_1(x)$ occur (Fig. 4). For $\sigma_1 < \sigma < \sigma_2(\tau)$, model solutions tend asymptotically to $T_1(x)$. No other behavior occurs unless τ is large enough, $\tau_1 < \tau$. Clearly one has $500 < \tau_1 < 1000$ years. For $\sigma_2 < \sigma < \sigma_3(\tau)$, large-amplitude oscillations (Fig. 6) between climate 1 and climate 3 occur. Finally, for $\sigma_3 < \sigma$, small-amplitude oscillations [$O(0.1 \text{ K})$] around $T_3(x)$ occur.

bations of the initial data segment $0 \leq t < 2\tau$, $T'(x, t) = T_3(x) + \theta(x)$, where $\theta(x)$ can be a constant or a random function of x , for $|\theta(x)| \leq 2 \text{ K}$. To discuss these types of behavior and compare them with those before, we return to the variational interpretation (7) of Eq. (4).

5) GEOMETRIC INTERPRETATION OF OSCILLATIONS

In Section 4a we considered the consequences of introducing delays into a dynamical system whose attractor set is made up only of isolated equilibria. It was shown that for a system with a single stable equilibrium, a delay can introduce an inertial effect which destabilizes the equilibrium, leading to oscillations around it.

The structure of the dynamical system governed by Eqs. (4)–(6) is considerably richer than Eq. (9). Still the presence of the variational principle (7) allows a heuristic interpretation of results by drawing on the analogy with the Lagrangian mechanics (14) for Eq. (13). It is useful in the present discussion to recall also the geometric interpretation in Section 3b for the results of the model without delays. In the following, we shall call the cauldron of (7) around $T_1(x)$ cauldron A, and that around $T_3(x)$ cauldron C.

It appears, even in the presence of delays, that all trajectories starting in cauldron A tend asymptotically to $T_1(x)$. For the linear ODE (9), the stably decaying or steadily oscillating character of solutions depended only on the value of the discrete delay τ , and not on the initial energy $\mathcal{E}_0 = \{u^2(0) + u^2(-\tau)\}/2$. On the other hand, the oscillations

were structurally unstable, since they obtained only for $\tau = \pi/2$.

For our nonlinear PDE (4) with distributed delay given by (6) as a function of (τ, σ) , oscillations seem to depend both on the parameter values and on the initial data segment $(T(x, t), \alpha[x, T(x, t)])$ for $0 \leq t < 2\tau$. They are structurally stable, since the existence of the oscillations persists and their character changes smoothly over wide ranges of (τ, σ) . Such stabilization by nonlinearity has already been alluded to in Section 3b and is common in the theory of nonlinear vibrations.

The oscillations around $T_1(x)$ obtain for a whole range of distributed delays (τ, σ) , but their initial "energy" has to be high: the initial data segment has to be in cauldron C. Indeed, the pass, or saddle point, between cauldrons A and C is at the point $T_2(x)$. We saw that both initial data with $T(x, 0) = T_1(x) + T_0$, $-10 \text{ K} \leq T_0 \leq -7.5 \text{ K}$, and initial data around $T_3(x)$, $T(x, 0) = T_3(x) + \theta(x)$, $|\theta(x)| \leq 2 \text{ K}$, resulted in trajectories crossing into cauldron A, where they either performed sustained oscillations or decayed to $T_1(x)$, according to the value of (τ, σ) . We have not studied the precise shape of cauldrons A and C, nor the neighborhood of the pass $T_2(x)$, but $\bar{T}_2 \approx 281.7 \text{ K} \approx \bar{T}_3 + 8.7 \text{ K} \approx \bar{T}_1 - 4.9 \text{ K}$ (Table 3). The interpretation that initial data have to be beyond the pass for oscillations in cauldron A to obtain is therefore rather plausible.

The oscillations within cauldron A were stable for perturbations in their asymptotic regime, $T'(x, t_1) = T(x, t) + \theta(x)$, and $\theta(x) = T_0 \leq -7.5 \text{ K}$, in accordance with the discussion for initial data. When $\theta(x)$ was a random function of x , stability depended on the mean and variance of θ . Results were again consistent with the idea that perturbations which took the trajectory sufficiently far, beyond the pass and into cauldron C, lead to renewal of the oscillations. Perturbations which involved a restart within cauldron A lead to a trajectory which eventually decayed to $T_1(x)$.

The behavior of solutions starting at $T_3(x)$ or near it which, for a certain (τ, σ) range, alternate between cauldron A and cauldron C is also mathematically interesting. They correspond to climate variations which are unrealistically large. Similarities exist, however, with solutions of the Lorenz (1963) model and of other dynamical systems with strange attractors. Hence their study might help the understanding of the more unusual strange attractor lying entirely within cauldron A. This study might be facilitated by the presence of the variational principle (7), not available for the Lorenz system or other known strange attractors, and by the geometric interpretations of some aspects of trajectories which it permits.

As a first step in investigating the connection be-

tween the large-amplitude and small-amplitude irregular oscillations, we considered solutions for a different value of μ . In Section 3b, the changes in the potential $J\{T(x); \mu\}$ with μ were described. Cauldrons A and C coalesce for a value of $\mu = \mu_1$; at this value, one would expect all small-amplitude oscillations occurring asymptotically within cauldron A, as well as the large-amplitude oscillations between cauldrons A and C, to disappear.

Numerical experiments were performed for $\mu = \mu_* = (1 + \mu_1)/2$, half-way between the present-day insolation conditions, $\mu = 1$, for which all other experiments were made, and $\mu = \mu_1$, at which all the trajectories which spend all or part of the time in cauldron A would disappear.

One experiment was done with $\mu = \mu_*$, the same parameter values as the one plotted in Fig. 4c, $\tau = 1000$ years, $\sigma = 100$ years, and the same initial data. The same type of small-amplitude, regular oscillation around $T_1(x)$ obtained. Its peak-to-peak amplitude in global temperature $\bar{T}(t)$ was $A = 1.22 \text{ K}$, as compared to $A = 0.83 \text{ K}$ (cf. Fig. 3) for $\mu = 1$. Results with other initial data in cauldron C were identical; they changed only very slightly when the lag parameters were modified a little, $\sigma = 60$ years and the same τ , for instance.

In other words, the flattening of the bottom of cauldron A has a tendency first to increase the amplitude of the periodic oscillations, without changing their character. This increase in amplitude as μ decreases is in agreement with the prevailing intuition that glaciation cycles have higher amplitude when the global ice volume is higher on the average (Källén *et al.*, 1979). As the insolation decreases, $\mu < 1$, the average temperature \bar{T}_1 decreases, and the ice volume increases correspondingly.

Next an experiment was performed with $\mu = \mu_*$, $\tau = 1500$ years, $\sigma = 1000$ years and initial data near $T_3(x)$. Large-amplitude, irregular oscillations result (Fig. 7a). The general character and the amplitude of the oscillations is similar to that for $\mu = 1$ (Fig. 7b). Notice, however, that two warm spikes are always present next to each other in Fig. 7b, somewhat like that in Fig. 6. In Fig. 7a, the pairs of spikes are replaced by a single warm spike, and the system spends more time in cauldron C than in cauldron A.

These results are merely indicative of the possible changes in the shape and nature of the attractor set as μ is varied. A detailed, exhaustive study would be interesting, but beyond our purpose here.

5. Discussion and conclusions

We have presented a simple energy-balance, Sellers-type climate model (EBM), in which a crude parameterization of the albedo effects of storm tracks along the ice margin was attempted. The model is

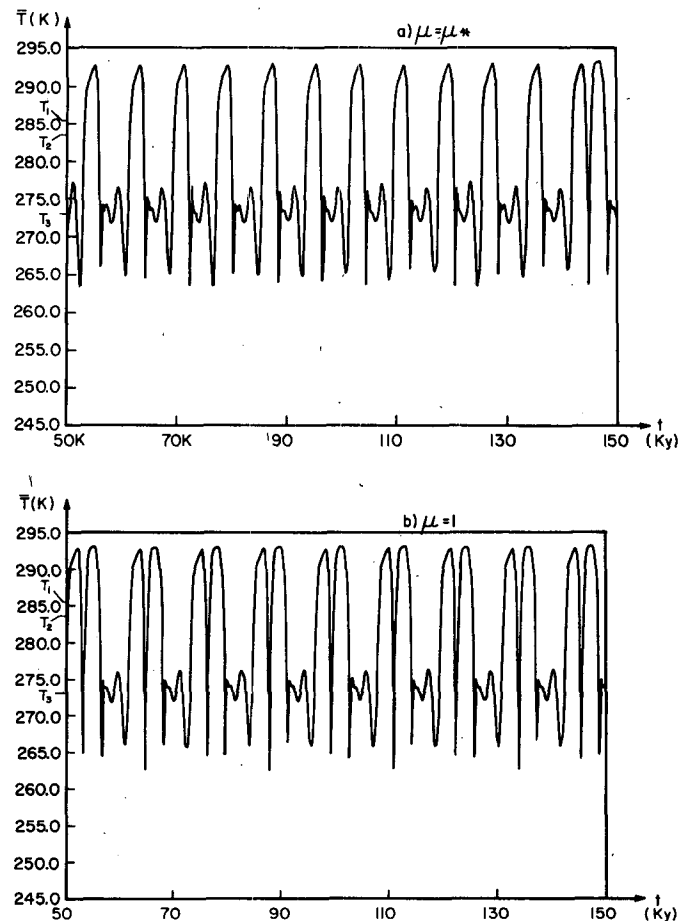


FIG. 7. Comparison of large-amplitude, irregular oscillations for two values of the heating parameter, $\mu = \mu^*$ (Fig. 7a) and $\mu = 1$ (Fig. 7b, see text for details). The oscillations are quite similar, but when μ is lowered below its present-day value, $\mu^* < 1$, the time the system spends at lower temperatures is increased. Lag parameter values are $\tau = 1500$ years, $\sigma = 1000$ years in both Figs. 7a and 7b.

governed by a nonlinear, parabolic PDE for zonally-averaged surface temperature T as a function of time t and colatitude ϕ , $T = T(\phi, t)$. The main nonlinearity is related to the *albedo-temperature feedback*, $\alpha = \alpha(x, T(x, t))$.

This nonlinearity results in EBM's exhibiting a *multiplicity of steady states*, at least two of which are stable: one corresponding to the present, observed climate of the Earth, with a globally averaged temperature $\bar{T}_1 \approx 287$ K; the other to a completely ice-covered Earth, $\bar{T}_3 \approx 175$ K (Held and Suarez, 1974; North, 1975; Ghil, 1976, 1981a). As a result of the albedo increase produced by cloudiness in the intense baroclinicity belt equatorward from the ice margin, the present model exhibits an *additional stable steady state*, with $\bar{T}_3 \approx 273$ K, lying between the "present" climate, $T_1 = T_1(\phi)$, and the "deep-freeze" climate, $T_5 = T_5(\phi)$.

In order to study long-term climate variability, on

the time scale of 10^3 – 10^5 years, the lag of ice-sheet extent and hence of albedo with respect to temperature (Källén *et al.*, 1979; Ruddiman and McIntyre, 1981) was introduced in the simplest way, as a distributed *time delay* in the governing equation, which thus becomes a functional or delay-differential equation. The combination of time-delay effects and of the relative closeness of the stable steady states $T_1(\phi)$ and $T_3(\phi)$ leads to very interesting model behavior. We suggest that system behavior of similar type can explain certain features of the observed spectrum of climatic variability on various time scales.

Observed spectra of climatic variance against frequency (e.g., Kutzbach and Bryson, 1974) have as their most striking features *peaks* of various bandwidths and heights on a *red-noise background*. Mitchell (1976) provided a tentative explanation for these two main features: the red-noise background was attributed to internal stochastic mechanisms,

whereas the peaks were attributed to external deterministic forcings. The simple generation of red noise by filtering white-noise input through a stable linear system was discussed by Hasselmann (1976) and Fraedrich (1978), among others.

The ratio in which variance is distributed between the continuous part of the spectrum and the peaks is uncertain, with estimates varying widely in each frequency band. Hays *et al.* (1976) assume that all the variance in the peaks between 10^3 and 10^6 years is due to orbital forcing only, with the result that 80% of the climatic variance within this band is in these peaks. Kominz *et al.* (1979), using cross-correlation spectra, have concluded that less than 25% of total variance in the same band is due to orbital forcing; the rest has to be due to other causes, which they assumed to be stochastic. A different interpretation for the superposition of broad peaks on a red-noise background can be given using the present model's results.

The model exhibits *self-sustained oscillations* without any variation in the external forcing, which is taken as the yearly averaged, constant solar insolation. These oscillations are due to the interaction between the model's heat capacity and its delay effects, coupled through the nonlinear ice-albedo feedback. The character of the oscillations changes as the ratio of the main delay time τ and of the relaxation time θ_d , governed by the heat capacity C_d , τ/θ_d changes. The existence and nature of the oscillations, quasi-periodic or aperiodic, also depends on the ratio of the distributed delay's half-width σ to its median value τ , σ/τ .

Oscillations with an amplitude A of approximately 1 K in global temperature \bar{T} occur in the neighborhood of model climate 1, for a large range of τ , $1000 \leq \tau < 3000$ years. This is a reasonably realistic amplitude for Pleistocene glaciation cycles (CLIMAP, 1976). The plateau of near constancy in $A = A(\tau)$ over the given range might be due to a phenomenon of *phase-locking* (Gollub and Benson, 1980; Libchaber and Maurer, 1980).

These oscillations do not appear when "warm" initial data, near the present climate or warmer, are used, or when correspondingly warm perturbations are applied to the oscillations once established. This is in accordance with the currently held belief about the absence of significant climatic oscillations during the relatively warm periods of the Earth's past.

In most previously studied EBM's, without cloud-albedo feedback and without delay effects, climatic evolution is restricted to the immediate vicinity of either stable steady state. Only large decreases of mean annual insolation can lead to a transition to colder climates, and a warming of the "deep freeze" is not possible with reasonable amounts of radiative energy. Within the present model, transitions from the colder stable climate $T_3(x)$ to the vicinity of the

warmer, present climate $T_1(x)$ are possible. Depending on the values of the delay parameters τ and σ a system state near climate 3 can lead to a climate evolution which either remains close to climate 3, or crosses over to the neighborhood of climate 1. The further evolution can, depending again on τ and σ , be either oscillation around or decay to climate 1.

The self-sustained oscillations around the present climate change in character from quasi-periodic to irregular, chaotic when τ increases beyond 3000 years, with some increase in amplitude. The Fourier spectrum of the *quasi-periodic* oscillations shows a number of high, narrow peaks on a low background noise. The dominant peak occurs at a frequency $f = f_0$ which is approximately equal to $1/(2\tau)$, with a number of harmonics to its right.

The transition to *aperiodicity* is accompanied by a general rise of the continuous part of the spectrum, with broadening and merging of most peaks. For $\tau = 5000$ and 10 000 years, only a few broad peaks on a very clear red-noise type spectrum remain. Indeed, in these figures, the log-log slope of the continuous spectrum to the right of the dominant, and down to a periodicity of 10 years, is -2 . This might indicate a relatively low *predictability* of climate on the decade-to-century time scale. Such a conclusion, if at all true, needs further verification by models incorporating a host of mechanisms with potential importance on these time scales, which were not included in the present model.

The range of τ for which moderate-amplitude, quasi-periodic as well as chaotic, model behavior obtains, seems to include values in agreement with both theory and observations. Phase lags between temperature and albedo which result when modelling explicitly ice-sheet response to energy balance (Källén *et al.*, 1979; Ghil and Le Treut, 1981) are of the order of 2000–3000 yr. Paleoclimatic data (Ruddiman and McIntyre, 1979, 1981) give slightly higher values of the order of 3000–5000 years. These discrepancies are well within the inaccuracies to be expected from relatively simple models and incomplete proxy data.

Considering the model's crudeness, the general similarity between the character of the spectra in Fig. 5 and of the spectra of paleoclimatic proxy data (Hays *et al.*, 1976, Fig. 6) is rather striking. Clearly, quasi-periodic orbital forcing on these time scales plays a role in climatic variability (Le Treut and Ghil, 1982), and so do numerous small-order effects which can be modeled collectively as white noise. Our results point to the potential contribution of simple deterministic nonlinear interactions between the most important mechanisms within the atmosphere-ocean-ice system to *both the peaks and the continuous background* in the climatic spectrum. The detailed study of simple models, selective confirmation of their results with more complex ones, and verifi-

cation by more refined data can confirm, modify or invalidate qualitative hypotheses like the one suggested by this study.

Acknowledgments. It is a pleasure to acknowledge interesting and useful discussions with H. Foley, A. Henderson-Sellers, B. Legras, J. London, J. Namias, G. R. North, E. L. Reiss, M. A. Ruderman, B. Saltzman, P. H. Stone, A. Suterà and D. L. Vulis. The interest, support and encouragement of James E. Hansen were crucial throughout the duration of the research. The comments of R. D. Cess, G. R. North and an anonymous third referee, contributed to the clarification of certain points in the text. One of us (M.G.) was partially supported by NASA Grant NSG-5130, monitored by the Laboratory for Atmospheric Sciences, Goddard Space Flight Center, and by NSF Grant ATM-80-18671, monitored by the Climate Dynamics Program. Computations were carried out at the Goddard Institute for Space Studies. The manuscript was patiently and cheerfully typed by Ilene Shifrin and Beth Duckett, and figures were drafted by Lilly Del Valle and Jose Mendoza.

APPENDIX A

Numerical Methods

a. Steady-state solutions

We outline first the numerical techniques used for computing steady-state solutions of Eq. (1a). Eq. (4), with $\partial T/\partial t = 0$, is solved subject to boundary conditions (5a,b). Details of the procedure for these steady-state computations appear in Ghil (1976).

The steady-state equation, after some rearrangement, can be written as a two-point boundary-value problem for the system of ordinary differential equations:

$$T_x = v, \quad (\text{A1.a})$$

$$v_x = -\left(\frac{\pi}{2}\right)^2 \frac{F(x, T)}{k(x, \tilde{T})} - \frac{\pi}{2} \left(\cot \frac{\pi x}{2}\right) v - \frac{k'_1(x) + k'_2(x)g(\tilde{T})}{k(x, \tilde{T})} v - \frac{k_2(x)g'(\tilde{T})}{k(x, \tilde{T})} v^2, \quad 0 < x < 1, \quad (\text{A1.b})$$

$$v(0) = v(1) = 0. \quad (\text{A2.a,b})$$

Here

$$k(x, \tilde{T}) = k_1(x) + k_2(x)g(\tilde{T}), \quad (\text{A3.a})$$

$$F(x, T) = \mu Q(x)\{1 - b(x) + c_1 \times [T_m + (T - c_2 z(x) - T_m)]\} - \sigma T^4 [1 - m \tanh(c_3 T^6)], \quad (\text{A3.b})$$

$\tilde{T} = \tilde{T}(x)$ is the data climate and $(\)' = d(\)/dx$. The numerical method of "shooting" (Isaacson and Keller, 1966; Keller, 1968) was used to solve the boundary-value problem (A1, A2): Eqs. (A1.a,b) are solved with initial conditions

$$v(0) = 0, \quad T(0) = T_0. \quad (\text{A4.a,b})$$

The solution of the initial-value problem (A1, A4) is denoted by $T(x, T_0)$, $v(x, T_0)$. Those values of T_0 which satisfy

$$v(1; T_0) = 0 \quad (\text{A5})$$

were next obtained by iteration. For these values of T_0 , the solution $T(x, T_0)$, $v(x, T_0)$ of the initial-value problem (A1, A4) is a solution of the boundary-value problem (A1, A2). Since $\cot(\pi x/2) \rightarrow \infty$ as $x \rightarrow 0$, Eq. (A1) is singular at the origin. The numerical difficulty arising from this singularity can be circumvented by using a variable-step method.

The initial-value problem (A1, A4) is solved to an accuracy of 10^{-7} using a variable time-step, variable-order, multi-step numerical scheme. The zeroes of $v(1; T_0)$ are found to an accuracy of 10^{-4} using the method of false positions or *regula falsi* (Isaacson and Keller, 1966). See Table 3 for solutions.

b. Time-dependent solutions without delay effects

We next describe the numerical method used to determine time-dependent solutions for the present model without time delays. The governing equation is Eq. (4), with $\alpha = \alpha(T; 0, 0)$, solved subject to initial and boundary conditions (5a,b,c). Eq. (4), with $K(x) \equiv \sin(\pi x/2)k[x, \tilde{T}(x)]$, can be written as

$$T_t = \frac{1}{C(x)} \left[\left(\frac{2}{\pi} \right)^2 \frac{1}{\sin(\pi x/2)} \times \{K(x)T_x\}_x + F(x, T) \right], \quad (\text{A6.a})$$

where subscripts denote partial derivatives with respect to the appropriate variables, and

$$F(x, T) = \mu Q(x)\{1 - \alpha(x, T)\} + c(T)\sigma T^4 \quad (\text{A6.b})$$

is given by (A3.b).

Let Δx and Δt be increments of the variables x and t , where $\Delta x = 1/(M-1)$, M being the number of spatial grid points used for computation. The set of points (x_j, t_n) in the (x, t) plane given by $x_j = (j-1)\Delta x$, $t_n = n\Delta t$, where $j = 1, 2, 3, \dots, M$ and $n = 0, 1, 2, \dots$, is the grid on which the finite-difference form of (A6) was computed by the time-marching procedure to be described below. The pole and the equator correspond to $j = 1$ and $j = M$, respectively. The approximation to $T(x_j, t_n)$ is denoted by T_j^n . The method closely follows the Crank-Nicholson scheme for nonlinear parabolic equations

as given in Richtmyer and Morton (1967, Chap. 8). It represents a considerable improvement in both accuracy and computing time over explicit schemes.

Using straightforward finite-difference approximation, Eq. (A6) is written as

$$\begin{aligned} \frac{T_j^{n+1} - T_j^n}{\Delta t} = & \left(\frac{2}{\pi}\right)^2 \frac{1}{\sin\left[\frac{\pi(j-1)}{2(M-1)}\right]} \\ & \times \frac{K_{j+1/2}(T_{j+1}^{n+1} - T_j^{n+1}) - K_{j-1/2}(T_j^{n+1} - T_{j-1}^{n+1})}{2C_j(\Delta x)^2} \\ & + \left(\frac{2}{\pi}\right)^2 \frac{1}{\sin\left[\frac{\pi(j-1)}{2(M-1)}\right]} \\ & \times \frac{K_{j+1/2}(T_{j+1}^n - T_j^n) - K_{j-1/2}(T_j^n - T_{j-1}^n)}{2C_j(\Delta x)^2} \\ & + \frac{F(x_j, T_j^n) + F(x_j, T_j^{n+1})}{2C_j}, \quad (A7) \end{aligned}$$

where $C_j = C(x_j)$. In Eq. (A7), the error terms originating from the finite-differencing have been dropped, leading to an error of $O\{(\Delta t)^2 + (\Delta x)^2\}$ in the approximate form (A7) of (A6). In other words, (A7) is a second-order accurate approximation to (A6). The numerical treatment of the nonlinear term arising from $F(x, T)$ will be described later. This is where our scheme differs slightly from the method in Richtmyer and Morton (1967, Sec. 8.5).

The linear terms in (A7) include values of T_j^q at $q = n$, as well as at $q = n + 1$. To advance in time from $q = n$ to $q = n + 1$, we have to find $\{T_j^{n+1}, j = 1, 2, \dots, M\}$.

Rearranging the linear terms in (A7) so that all T_j values at $q = n + 1$ are on the left-hand side, and denoting the remaining right-hand side by D_j^{n+1} , we obtain

$$\begin{aligned} T_{j+1}^{n+1}(-\gamma_j K_{j+1/2}) + T_j^{n+1}(1 + \gamma_j K_{j+1/2} + \gamma_j K_{j-1/2}) \\ + T_{j-1}^{n+1}(-\gamma_j K_{j-1/2}) = D_j^{n+1}, \quad (A8) \end{aligned}$$

where

$$\gamma_j = \frac{\Delta t}{2C_j(\Delta x)^2} \left(\frac{2}{\pi}\right)^2 \frac{1}{\sin\left[\frac{\pi(j-1)}{2(M-1)}\right]}.$$

The system of linear equations for the T_j^{n+1} represented by Eqs. (A8) is clearly tridiagonal. However, before the standard techniques for solving a tridiagonal system of simultaneous linear equations can be applied, the system of equations (A8) has to be arranged in such a way that the coefficient of T_1^{n+1}

in the first equation and the coefficient of T_M^{n+1} in the last equation vanish. This is very easily done with the help of the boundary conditions (Collatz, 1960, p. 264; Schneider and Gal-Chen, 1973):

$$\left. \begin{aligned} T_1 &= (4T_2 - T_3)/3 \\ T_M &= (4T_{M-1} - T_{M-2})/3 \end{aligned} \right\}, \quad (A9)$$

where the superscripts $n + 1$ in T_j^{n+1} are omitted as self-understood.

Eqs. (A9) are actually the second-order accurate finite-difference form of the requirement that heat fluxes vanish at the pole and also at the equator, i.e.,

$$T_x(x, t) = 0, \quad \text{at } x = 0 \text{ and } x = 1, \quad (5a, b)$$

for all values of time t . The tridiagonal system of simultaneous linear equations (A8) can be solved at each time step $q = n + 1$ to obtain $T_2, T_3, \dots, T_{M-2}, T_{M-1}$ by Gaussian elimination and back substitution.

Solving the tridiagonal system of simultaneous linear equations (A8) provides an exact solution $\{T_j^{n+1}\}$ of Eq. (A7) only if the right-hand sides D_j^{n+1} of the equations in (A8) are actually known, independently of the T_j^{n+1} 's. However, a comparison of Eqs. (A7) and (A8) shows that each D_j^{n+1} is the sum of a linear part L_j^n given by

$$\begin{aligned} L_j^n = & T_j^n + \gamma_j K_{j+1/2}(T_{n+1}^n - T_j^n) \\ & - \gamma_j K_{j-1/2}(T_j^n - T_{j-1}^n), \quad (A10.a) \end{aligned}$$

and of a nonlinear part $G_j^{n,n+1}$ given by

$$G_j^{n,n+1} = \frac{1}{2C_j} (F_j^n + F_j^{n+1}), \quad (A10.b)$$

where $F_j^q = F(x_j, T_j^q)$.

Due to the presence of the nonlinear part, a *predictor-corrector* approach was adopted in going from one time step to the next. For each iteration at a given mesh point, the known linear part was kept the same. The nonlinear part was iterated upon until a given convergence criterion was achieved; the criterion chosen was that the absolute error in temperature at each mesh point not exceed 10^{-5} . Specifically, the *predictor* equation used was

$$T_j^p = T_j^n + \gamma_j \{(KT_x)_x|_j^n + (KT_x)_x|_j^p\} + \Delta t F_j^n, \quad (A11)$$

and the *corrector* equation was

$$\begin{aligned} T_j^c = & T_j^n + \gamma_j \{(KT_x)_x|_j^n + (KT_x)_x|_j^c\} \\ & + \frac{1}{2} \Delta t (F_j^n + F_j^p). \quad (A12) \end{aligned}$$

Here $(KT_x)_x|_j^q$, $q = n, p, c$, is expressed by central differences, as in (A7). Both (A11) and (A12) are rearranged as in (A8), resulting in tridiagonal linear systems for $\{T_j^p\}$ and $\{T_j^c\}$, respectively, with known right-hand sides.

After obtaining $T_2^p, T_3^p, \dots, T_{M-1}^p$ for the new

time step from (A11), T_j^l and T_M^l were obtained using the boundary conditions (A9). This procedure was repeated for $\{T_j^c: j = 1, 2, \dots, M\}$, using both (A12) and (A9), for the correction step. If the difference between T_j^c and T_j^l satisfied the convergence criterion, we set $T_j^{n+1} = T_j^c$, $j = 1, 2, \dots, M$. Otherwise, the correction step was repeated until convergence was achieved. Usually, not more than one or two correction steps were needed. When temperature variations were rapid, however, as many as 10 or 15 iterated corrections might be needed for the criterion to be satisfied.

For all time-dependent computations, a spatial grid size of 5° latitude was chosen after some numerical experimentation. For this grid size, each steady-state solution, when interpolated to the grid for time-dependent computation and used as an initial state, gave an asymptotic temperature distribution which is within 2 K of the original steady-state solution (Table 3). Furthermore, the computational effort for this grid size was not excessive.

The time step Δt was chosen to be five years. Here some experimentation was also necessary, because numerical instability of a nonlinear nature occurs for higher values of Δt , before the linear instability threshold is reached. This nonlinear instability manifests itself first at the boundaries, and propagates into the interior of the interval. It does not appear for the chosen values of Δt .

c. Time-dependent solutions with time delays

When time delays are introduced [$\alpha = \alpha^*(T^*, \tau, \sigma)$, $\tau \neq 0$] Eq. (4) becomes a *functional*, or delay differential equation (FDE or DDE). Such delay differential equations can be solved by the usual method of solving the corresponding ordinary or partial differential equations (Driver, 1977), except that in this case one has to specify an initial function over a finite time interval, rather than an initial value at a single instant.

For the present work, this initial function was not naturally specified in the problem; therefore, it had to be generated. This was done by carrying out the computation from $t = 0$ to $t = 2\tau$ with the albedo being determined by the present temperature (no delay), and using the computed temperatures to build up a "tail" which is 2τ time units long. This "tail" then provided the lagged temperature for all $t > 2\tau$, and was updated for all $t > 2\tau$. The computation of solutions proceeded in all other respects as before: the only modification appears in evaluating F_j^n and F_j^l in (A7)–(A12), using $\alpha^*(T^*)$ rather than $\alpha(T)$.

APPENDIX B

Spectral Analysis of Solutions

The need to estimate the *power spectrum* of a stationary stochastic process from a finite-length record

of a single realization arises in many applications (e.g., Blackman and Tukey, 1958; Jenkins and Watts, 1968). Depending on the area of application, the characteristics of the time series analyzed and the information required, various practical methods of harmonic analysis have been devised and tested. The purpose of this appendix is to clarify two points: 1) why this body of knowledge is relevant to the analysis of solutions to a *deterministic* model, and 2) which particular spectral analysis method was used in the present work. The second point is relatively trivial and included for documentation only; the first point is considerably deeper and one can only outline here its resolution.

a. Deterministic and stochastic time series

We start with a brief recapitulation of basic facts, following Hannan (1960, Chap. 1). It will shed some light on both the points to be clarified. For details we refer to the literature.

Consider a finite, periodic sequence of random variables $\{x_t(\omega): t = 0, 1, 2, \dots, n-1\}$, ω labeling the realization and n the period, i.e., $x_{t+n}(\omega) = x_t(\omega)$. This is the simplest possible *stochastic process*. The general case of a *discrete-time* stochastic process is obtained when $n \rightarrow \infty$, i.e., when the index t can be any integer. For a *continuous-time* process, t is any real number. These general cases present technical difficulties which will not be discussed.

The process $\{x_t(\omega)\}$ is assumed to have zero mean, finite variance and to be stationary, i.e., for all t and s ,

$$E\{x_t(\omega)\} = 0, \quad (\text{B1.a})$$

$$E\{x_t^2(\omega)\} < \infty, \quad (\text{B1.b})$$

$$E\{x_{t+s}(\omega)x_t(\omega)\} = R_s, \quad (\text{B1.c})$$

with the covariance R_s depending only on the separation s and not on the particular time t . Here E is the expectation operator or ensemble average over all realizations ω .

We define the *time-shift operator* U by

$$Ux_t(\omega) = x_{t+1}(\omega). \quad (\text{B2})$$

One introduces a vector space V in which the sequences $\{x_t\}$ live, and an inner product of sequences (Courant and Hilbert, 1953, Chap. 1) by taking the expected value over ω of the usual scalar product over indices t . Thus the orthogonality in V of the two sequences corresponds to their being probabilistically uncorrelated.

It is easily seen that, in the vector space V , the operator U is *unitary*: its adjoint is its inverse, and all its eigenvalues $\{\nu_j: j = 1, 2, \dots, n\}$ are therefore on the unit circle. More precisely, they are the roots of unity:

$$\nu_j = \exp\{2\pi i j/n\}, \quad (\text{B3})$$

where i is the imaginary unit. The eigenvectors are

mutually orthogonal, and we let P_j be the orthogonal projection onto the j th eigenvector.

Dropping for convenience the dependence on ω , one has

$$x_t = U^t x_0 = \sum_1^n \nu_j^t P_j x_0. \quad (\text{B4.a})$$

It is thus natural to let

$$Z_j = P_j x_0, \quad (\text{B4.b})$$

so that the inner product of Z_j and Z_k is

$$(Z_j, Z_k) = 0, \quad j \neq k. \quad (\text{B4.c})$$

In terms of these uncorrelated $\{Z_j\}$, the covariance function R_t becomes

$$R_t = \sum_1^n \nu_j^t S_j, \quad (\text{B4.d})$$

where

$$S_j = (Z_j, x_0) = E(|Z_j|^2) \geq 0. \quad (\text{B4.e})$$

To suggest the more general cases, we write

$$P(\nu) = \sum_{-i \log \nu_j \leq \nu + \pi} P_j, \quad (\text{B5.a})$$

$$Z(\nu) = \sum Z_j, \quad (\text{B5.b})$$

$$F(\nu) = \sum S_j, \quad (\text{B5.c})$$

where all the sums are taken over those j which satisfy $2\pi j/n \leq \nu + \pi$. Notice that, due to (B4.e), $F(\nu)$ is monotone increasing. With this notation, one obtains the spectral representations

$$U = \int_{-\pi}^{\pi} e^{i\nu} dP(\nu), \quad (\text{B6.a})$$

$$x_t = \int_{-\pi}^{\pi} e^{it\nu} dZ(\nu), \quad (\text{B6.b})$$

$$R_t = \int_{-\pi}^{\pi} e^{it\nu} dF(\nu), \quad (\text{B6.c})$$

$$(Z(\nu), Z(\nu)) = F(\nu), \quad (\text{B6.d})$$

$$[Z(\nu_1) - Z(\nu_2), Z(\nu_3) - Z(\nu_4)] = 0,$$

$$\text{for } \nu_1 \geq \nu_2 > \nu_3 \geq \nu_4. \quad (\text{B6.e})$$

In the elementary case of a periodic sequence $\{x_t; t = 0, 1, \dots, n-1\}$, Eqs. (B6) are just a rewriting of (B4) with the notation (B5). The point is that (B6) still holds for the general discrete-time stochastic process; in the continuous-time case of random functions on the real line, the limits of integration must be changed from $\pm\pi$ to $\pm\infty$.

Thus, in all cases, the Fourier-Stieltjes transform (B6.b) of the stochastic process x_t itself is connected via (B6.d) with the spectral decomposition (B6.c) of its covariance function R_t into "independent oscillations," cf. (B6.e). They are both based on the spectral representation (B6.a) of the unitary shift operator U .

For deterministic processes, the label ω , which

characterizes a realization of the process in the stochastic case, can be replaced by the initial state, \bar{T} ($t = 0$) say. Ensemble averaging over realizations ω is replaced by averaging over possible initial states. An individual time series segment will still look, for a complex deterministic evolution law, as different from another segment of the same series, or from a time series evolving from another initial state, as if it were random. Still, all time series, independently of $\bar{T}(0)$, have certain things in common.

To capture the common features of all individual evolutions of a deterministic process, one defines an appropriate shift operator, similar to (B2). The properties of such shift operators, in both deterministic situations and probability spaces, are the object of *ergodic theory* [see, e.g., Moser (1973, Sec. 1.4 and Chap. 3) for the connection between the two cases, and Hannan (1960, Sec. 2.2) for more details on the probabilistic case]. In particular, the spectral representation of the deterministic shift operator leads to the spectral analysis of the associated time series, in a manner entirely analogous to the situation for stochastic processes described above.

Intuitively, the deterministic picture is the following. All initial data lead, after a certain time interval of transient behavior, to a trajectory lying on the attractor set. When this attractor set is a limit cycle, trajectories only differ by their phase along the cycle. Thus, one can define an invariant measure, or "probability density function," on the limit cycle, and the situation is quite analogous to that described by Eqs. (B1)–(B4). The precise probability density on the limit cycle will depend on the distribution of initial data which lead to a particular phase of the limiting trajectory.

When the limiting solutions are quasi-periodic, rather than purely periodic, one defines a probability density on the torus which constitutes the attractor set. Again, the relative "weight" of various portions of the surface of the torus depends on which initial data are attracted to that portion of the surface. The limit cycle case and torus case cover the situation in Figs. 4a–c.

When the attractor set is strange (Figs. 4e, 4f), the situation is somewhat more complex. Indeed, strange attractors have a complicated geometry (Lorenz, 1963; Ruelle, 1980): they are made up of infinitely many "sheets" packed close to each other, like onion skin, and "sown together" along common edges. The effort to define appropriate invariant measures for them is currently under way (Graham and Scholz, 1980). In the following, the language of random time series will be borrowed for convenience, since it is more familiar; only occasional references will be made to the deterministic situation at hand.

b. Spectral windows

We are ready to turn now to the details of the spectral analysis of model solutions. First, the non-

decreasing, deterministic function $F(\nu)$ of (B6.c) is more convenient to work with than the random function $Z(\nu, \omega)$ of (B6.c). In most cases of practical interest, $F(\nu)$ can be decomposed into two parts

$$F = F_1 + F_2; \quad (\text{B7.a})$$

a continuous part

$$F_1(\nu) = \int_{-\infty}^{\nu} S(\nu) d\nu, \quad (\text{B7.b})$$

and a pure-jump part $F_2(\nu)$, constant save for jumps at discrete frequencies ν_k . If only F_2 is present the process has a *discrete spectrum*, given by $\{\nu_k\}$ and the associated jumps $\{F(\nu_k+) - F(\nu_k-)\}$. If only F_1 is present, the process has a purely *continuous* spectrum with *spectral density* $S(\nu)$. In ours, as in most cases, the spectrum is mixed. Moreover, based on a finite-length time series with limited resolution, pure jumps are hard to identify and become translated into more or less sharp *peaks* of the spectral density (recall that the derivative of a Heaviside step function is a Dirac δ -function). It is customary, therefore, to deal, for all processes having absolutely-integrable covariance R_t , with the spectral density $S(\nu)$ only. We shall do so in the sequel [but see also Hannan (1960, Sec. 4.1)].

The Bochner-Khinchin theorem states that, in the general discrete-time and continuous-time cases, the covariance function R_t has a Fourier-Stieltjes transform $dF(\nu)$. In particular, in the continuous-time, continuous-spectrum cases which we consider, it follows that the true spectral density of the process, which we shall denote by $\tilde{S}(\nu)$, i.e.,

$$\tilde{S}(\nu) = \frac{1}{2\pi} \int_{-\infty}^{\infty} e^{-i\nu s} R_s ds, \quad (\text{B8})$$

is non-negative since $\tilde{F}(\nu)$ is nondecreasing.

Given a realization of the process $x_t(\omega)$, and a record of it of length L , one can compute a sample correlogram $R_L(s)$ and its Fourier transform $S_L(\nu)$. The unfortunate fact is that the sample *periodogram* $S_L(\nu)$ is not a *consistent estimate* of $\tilde{S}(\nu)$, i.e., it is not true that

$$S_L(\nu) \rightarrow \tilde{S}(\nu) \text{ as } L \rightarrow \infty. \quad (\text{B9.a})$$

That is, (B9.a) does not hold in general in *any* sense of probabilistic convergence (Hannan, 1960, Chap. 3; Parzen, 1961) for all frequencies, neither in mean square, nor in probability or in distribution.

In practice, a periodogram taken from one realization of a stochastic process and from another one will be widely different. For a given realization, or time series, the periodogram $S_L(\nu)$ will show large dispersion at every frequency as L is increased, with no signs of convergence. The same statement holds for sufficiently complex deterministic time series, with which we are concerned here, i.e., large discrepancies

between a periodogram $S_L(\nu)$ of the series and its actual spectral density $\tilde{S}(\nu)$ occur, no matter how long L is.

Fortunately, it is true that R_L is a consistent estimate of the true covariance function \tilde{R} , i.e.,

$$\lim_{L \rightarrow \infty} E\{|R_L(\nu) - \tilde{R}(\nu)|^2\} = 0, \quad (\text{B9.b})$$

$$\text{Prob}\{\lim_{L \rightarrow \infty} R_L(\nu) = \tilde{R}(\nu)\} = 1, \quad (\text{B9.c})$$

both hold. Moreover, one can show from (B9.b,c) that situation (B9.a) can be remedied by introducing an averaging kernel $K_L(\nu)$. In fact, for any bounded continuous kernel $K(\nu)$, the spectral average estimate $\hat{S}_L(\nu; K)$,

$$\hat{S}_L(\nu; K) = \int_{-\infty}^{\infty} K(\nu) S_L(\nu) d\nu, \quad (\text{B10})$$

tends to $\tilde{S}(\nu)$ as $L \rightarrow \infty$, both in mean square [as in (B9.b)] and in probability [as in (B9.c)].

Usually, the kernel $K(\nu)$ is chosen to be symmetric about the frequency at which it has its (unique) absolute (positive) maximum. This frequency is called the peak frequency of the kernel $K(\nu)$. Its *bandwidth* $\beta(K)$ is the length of the square with the height of the peak and the same total area as $K(\nu)$. Kernels used in practice are largely concentrated near their peak and are therefore also called a *spectral window*. The bandwidth $\beta(K)$ is essentially the resolution of the spectral density estimate $\hat{S}_L(\nu; K)$. The smallest possible resolution of a spectral estimate \hat{S}_L can be shown to be of the order of $1/L$.

The smoothing of the periodogram $S_L(\nu)$ by a spectral window $K_L(\nu)$ in the frequency domain is equivalent to the smoothing of the correlogram $R_L(\nu)$ by the Fourier transform of $K_L(\nu)$, $k_L(s)$ say, in the time domain. This $k_L(s)$ is the covariance averaging kernel or *lag window* for short. We used the centered sample covariance function

$$R_L(s) = \begin{cases} \frac{1}{L} \int_0^{L-|s|} (\bar{T}(t+|s|) - T_m)(\bar{T}(t) - T_m) dt, & |s| < L \\ 0, & |s| \geq L, \end{cases} \quad (\text{B11})$$

where T_m is the mean value of the time series $\bar{T}(t)$ for $0 \leq t \leq L$.

Since $\bar{T}(t)$ is a real time series, its spectral density $\tilde{S}(\nu)$ is an even function of ν and the Fourier transform in (B8) can be replaced by a cosine transform. Therefore, the lag-averaged, normalized estimate of $\tilde{S}(\nu)$ we used was

$$\hat{S}_L(\nu) = \frac{2}{\pi R_L(0)} \int_0^L \cos(\nu s) k_L(s) R_L(s) ds. \quad (\text{B12})$$

The numerical method used to compute the integral above follows Vulis and Monin (1979), in order to avoid the problem of negative spectral estimates; unless suitable precautions are taken, this problem occurs often in practice.

The lag window $k_L(s) = k_L(s; M)$ due to Bartlett is

$$k_L(s; M) = \begin{cases} 1 - |s|/M, & |s| < M \\ 0, & |s| \geq M; \end{cases} \quad (\text{B13})$$

it depends on the parameter M , where M is the maximum lag retained in the correlation $R_L(s)/R_L(0)$. It is easy to show that the use of the Bartlett filter is equivalent to subdividing a record of length L into $l = L/M$ segments of length M , calculating the l separate periodograms and averaging them to obtain $\hat{S}_L(\nu)$.

The variance of the estimate $\hat{S}_L(\nu)$ is inversely proportional to the rate at which the filter $k_L(s)$ concentrates at the origin, i.e.,

$$\frac{\text{Var}[\hat{S}_L(\nu)]}{\hat{S}(\nu)} = \frac{\int_0^L k_L^2(s) ds}{L}. \quad (\text{B14})$$

Using the Bartlett filter, one can reduce the variance of $\hat{S}_L(\nu; M)$ to equal $1/3(M/L)$ of the variance of the "naive" periodogram S_L . This would suggest taking M as small, or l as large as possible.

Unfortunately, an "uncertainty principle" obtains; namely the product of $\text{Var}(\hat{S}_L)$ and of the bandwidth $\beta(K_L)$ is a constant: the accuracy of locating a spectral peak and that of measuring its height have to be traded off against each other. It is therefore customary to do some numerical experimentation and use different values of M . This practitioner's art is called "window closing" or "opening" (Jenkins and Watts, 1968, Sec. 7.2). The limitation on bandwidth resolution justifies now more rigorously the earlier decision not to deal explicitly with the pure-jump part $F_2(\nu)$ of the spectral distribution function in (B7).

c. Technical details

The time series used were of various lengths. In all cases, an initial segment was eliminated, so that only the asymptotic behavior of the solution appeared in the spectral analysis.

For the case $\tau = 500$ years (Figs. 4a and 5a), a record extending from $t = 25\,000$ to $100\,000$ years was used, so that $L = 75\,000$ years. For $\tau = 1500$ years (Figs. 4d and 5d), the record had the same length, but started at $t = 50\,000$ years. For $\tau = 750$, 1000 and 5000 years (Figs. 5b, 5c and 5e), the records started at 50 000 years and $L = 150\,000$ years. For $\tau = 10\,000$ years (Fig. 5f), the record used started at $t = 100\,000$ years and had $L = 300\,000$ years.

TABLE A1. Confidence intervals $[A_1(\mu, \alpha), A_2(\mu, \alpha)]$ for spectral density estimates.*

μ	A_1	$\log_{10} A_1$	A_2	$\log_{10} A_2$
15	0.55	-0.26	2.3	0.36
30	0.63	-0.20	1.8	0.26

* The values in the table correspond to a 95% confidence level, or $\alpha = 0.05$; μ is the equivalent number of degrees of freedom of a χ_μ^2 -distribution (see text for details).

The time step used in sampling equaled in all cases $\Delta t = 5$ years. The Nyquist frequency f_N therefore equals $f_N = 1/10 \text{ year}^{-1}$. The frequency corresponding to the maximum lag of the correlation function equals to $f_M = 1/M$. Fig. 5 shows the spectral density estimates $\hat{S}_L(\nu; M)$ between f_N and $10^{-2} \text{ year}^{-1} < f_N$; for periods < 100 years, model assumptions become somewhat questionable. Notice that in the figure, as in the main text, we have denoted frequency by f , rather than ν .

The bandwidth $\beta(K_L(\nu; M))$ for the Bartlett filter is obtained by taking the Fourier transform of (B13) and equals $1/2M$ (Jenkins and Watts, 1968, Tables 6.5 and 6.6 and Fig. 6.11). In Figs. 5a–5e, $M = L/5$, while in Fig. 5f, based on a much longer time series, $M = L/10$; thus $\beta = 10^{-4} \text{ year}^{-1}$ in Figs. 5a and 5d, and $\beta = 0.5 \times 10^{-4} \text{ year}^{-1}$ in Figs. 5b, 5c, 5e and 5f.

In the logarithmic frequency scale of Fig. 5, the bandwidth is interpreted as

$$\begin{aligned} \log(\nu + \Delta\nu) - \log\nu &= \log((\nu + \Delta\nu)/\nu) \\ &= \log(1 + \Delta\nu/\nu) \approx \Delta\nu/\nu = \beta/\nu. \end{aligned} \quad (\text{B15})$$

Thus the relative resolution improves toward higher frequencies.

The accuracy of the spectral estimate at fixed ν is given by its variance [Eq. (B14)]. An important statistical tool in the analysis of variance is the χ_μ^2 distribution for sums of squares of μ independent normal random variables. It can be shown that for the periodogram itself as a spectral estimator, $2S_L(\nu)/\hat{S}(\nu)$ is distributed approximately like the sum of two such squares, $\mu = 2$. For a rectangular (box-car) lag window, the number of "degrees of freedom" μ is $\mu = L/M$, exactly equal to the number of "independent samples" (compare Leith, 1973). For the Bartlett lag window, $\mu\hat{S}_L(\nu; M)/\hat{S}(\nu)$ is distributed like χ_μ^2 with the equivalent number of degrees of freedom $\mu = 3L/M$ (Jenkins and Watts, Sec. 6.3.5 and 6.4.2, and Table 6.6).

Based on the cumulative probability distribution $F = F_\mu(x)$ of the variable $x = \chi_\mu^2$, one can give confidence intervals on $\hat{S}_L(\nu)$ of the form

$$\begin{aligned} \text{Prob}\{x_\mu(\alpha/2) < \mu\hat{S}_L(\nu)/\hat{S}(\nu) \\ < x_\mu(1 - \alpha/2)\} = 1 - \alpha. \end{aligned} \quad (\text{B16.a})$$

Here $x_\mu(\gamma)$ refers to tabulated values of the solution

to the equation $F_\mu(x) = \gamma$. This solution is unique since $F_\mu(x)$ is monotone increasing. Given the estimate $\hat{S}_L(\nu)$, the true spectral density $\hat{S}(\nu)$ will then lie with a confidence of $100(1 - \alpha)$ percent between $A_1\hat{S}_L(\nu)$ and $A_2\hat{S}_L(\nu)$, where

$$A_1(\mu, \alpha) = \frac{\mu^S L(\nu)}{x_\mu(1 - \alpha/2)},$$

$$A_2(\mu, \alpha) = \frac{\mu^S L(\nu)}{x_\mu(\alpha/2)}. \quad (\text{B16})$$

The narrowing of the confidence interval (A_1, A_2) as μ and α increase is easily seen for instance in Jenkins and Watts (1968, Fig. 3.10).

The application of these ideas to our model solutions is justified by the fact that typical correlation times for these solutions are much shorter than the lag times M which were used. In Figs. 5a–5e, $M = L/5$ and thus $\mu = 15$; in Fig. 5f, $M = L/10$ and $\mu = 30$. The corresponding values of A_1 and A_2 for a 95% confidence level are given in Table A1. They are also indicated in Figs. 5a–5f by a double arrow, and hold uniformly for all frequencies.

The estimates of spectral density in Figs. 5a–5f, and of the location of the peaks in Table 4 are stable. Different values of M and of spectral resolution in plotting produce the expected changes: larger M leads to a smoother spectrum, with broader bandwidth and smaller peaks. The changes, however, are quite small; the largest observed change in the location of a peak, for instance, is 0.3% when M was doubled.

The smaller, broader peaks in Fig. 5, which appear as undulations between those peaks identified as kf_0 , are probably produced by the “side lobes” of the Bartlett spectral window (Jenkins and Watts, 1968, Fig. 6.11). They could be eliminated by a more careful selection of the window (*ibid.*, Table 6.5 and Figs. 6.12, 6.13) or of the sampling interval. Such “window carpentry” did not seem necessary in our application, since the main features of the spectra, namely their quasi-periodic or aperiodic character, are already evident in Figs. 5a–f.

REFERENCES

- Alexander, R. C., and R. L. Mobley, 1974: *Monthly Average Sea-Surface Temperatures and Ice-Pack Limits on a 1° Global Grid*. Rep. R-1310-ARPA, Rand Corp., Santa Monica, 30 pp. [NTIS AD A008575].
- Benzi, R., G. Parisi, A. Suter and A. Vulpiani, 1982: Stochastic resonance in climatic change. *Tellus*, **34**, 10–16.
- Berry, F. A. Jr., E. Bollay and N. R. Beers, Eds., 1945: *Handbook of Meteorology*. McGraw-Hill, 1068 pp.
- Bhattacharya, K., and M. Ghil, 1978: An energy-balance model with multiple-periodic and quasi-chaotic free oscillations. *Evolution of Planetary Atmospheres and Climatology of the Earth*, Centre National d'Études Spatiales, Toulouse, 299–310.
- , 1979: *A study of almost-intransitivity as a possible cause of terrestrial climate changes*. Ph.D. thesis, Columbia University, 161 pp.
- Birchfield, G. E., and J. Weertman, 1978: A note on the spectral response of a model continental ice sheet. *J. Geophys. Res.*, **83C**, 4123–4125.
- Blackman, R. B., and J. W. Tukey, 1958: *The Measurement of Power Spectra from the Point of View of Communications Engineering*. Dover, 190 pp.
- Budyko, M. I., 1972: The future climate. *Trans. Amer. Geophys. Union*, **53**, 868–874.
- Cahalan, R. F., and G. R. North, 1979: A stability theorem for energy-balance climate models. *J. Atmos. Sci.*, **36**, 1178–1188.
- Cess, R. D., 1976: Climate change: An appraisal of atmospheric feedback mechanisms employing zonal climatology. *J. Atmos. Sci.*, **33**, 1831–1843.
- , 1978: Biosphere-albedo feedback and climate modeling. *J. Atmos. Sci.*, **35**, 1765–1768.
- CLIMAP Project Members, 1976: The surface of the ice-age earth. *Science*, **191**, 1131–1137.
- Collatz, L., 1960: *The Numerical Treatment of Differential Equations*, 3rd ed. Springer-Verlag, 568 pp.
- Courant, R., and D. Hilbert, 1953: *Methods of Mathematical Physics*, Vol. 1. Wiley-Interscience, 559 pp.
- Crafoord, C., and E. Källén, 1978: A note on the condition for existence of more than one steady-state solution in Budyko-Sellers type models. *J. Atmos. Sci.*, **35**, 1123–1125.
- Dansgaard, W., S. J. Johnsen, H. B. Clausen and C. C. Langway, Jr., 1971: Climatic record revealed by Camp-Century ice-core. *The Late Cenozoic Glacial Ages*, K. Turekian, Ed., Yale University Press, 267–306.
- Driver, R. D., 1977: *Ordinary and Delay Differential Equations*. *Appl. Math. Sci.*, Vol. 20, Springer-Verlag, 501 pp.
- Duplessy, J. C., G. Delibrias, J. L. Turon, C. Pujol and J. Duprat, 1981: Deglacial warming of the northeastern Atlantic Ocean. Correlation with the paleo-climatic evolution of the European continent. *Paleogeogr., Paleoclim., Paleoecol.*, **35**, 121–144.
- Farmer, J. D., 1982: Chaotic attractors of an infinite dimensional dynamical system. *Physica*, **4D**, 366–393.
- Fraedrich, K., 1978: Structural and stochastic analysis of a zero-dimensional climate system. *Quart. J. Roy. Meteor. Soc.*, **104**, 461–474.
- Gal-Chen, T., and S. H. Schneider, 1976: Energy balance climate modeling: Comparison of radiative and dynamic feedback mechanisms. *Tellus*, **28**, 108–121.
- Gates, W. L., and A. B. Nelson, 1975: *A New (revised) Tabulation of the Scripps Topography on a 1° Global Grid. Part II: Ocean Depths*. Rep. R-1277-1-ARPA, Rand Corp., Santa Monica, 132 pp. [NTIS AD A017567].
- Ghil, M., 1976: Climate stability for a Sellers-type model. *J. Atmos. Sci.*, **33**, 3–20.
- , 1981a: Energy-balance models: An introduction. *Climatic Variations and Variability: Facts and Theories*, A. Berger, Ed., D. Reidel, 461–480.
- , 1981b: Internal climatic mechanisms participating in glaciation cycles. *Climatic Variations and Variability: Facts and Theories*, A. Berger, Ed., D. Reidel, 539–557.
- , and K. Bhattacharya, 1979: An energy-balance model of glaciation cycles. *Report of the JOC Study Conference on Climate Models: Performance, Intercomparison and Sensitivity Studies*, GARP Publ. Ser., No. 22, WMO/ICSU, 886–916.
- , and H. Le Treut, 1981: A climate model with cryodynamics and geodynamics. *J. Geophys. Res.*, **86C**, 5262–5270.
- Goldstein, H., 1980: *Classical Mechanics*. Addison-Wesley, 672 pp.
- Gollub, J. P., and S. V. Benson, 1980: Many routes to turbulent convection. *J. Fluid Mech.*, **100**, 449–470.
- Goody, R., 1980: Polar processes and world climate (a brief overview). *Mon. Wea. Rev.*, **108**, 1935–1942.
- Graham, R., and H. J. Scholz, 1980: Analytic approximation of

- the Lorenz attractor by invariant manifolds. *Phys. Rev.*, **A22**, 1198–1204.
- Hale, J., 1971: *Functional Differential Equations*. Springer-Verlag, 238 pp.
- , 1977: *Theory of Functional Differential Equations*. *Appl. Math. Sci.*, Vol. 3, Springer-Verlag, 365 pp.
- Hannan, E. J., 1960: *Time Series Analysis*. Methuen and Barnes and Noble, 152 pp.
- Hasselmann, K., 1976: Stochastic climate models I. Theory. *Tellus*, **28**, 473–485.
- Hays, J. D., J. Imbrie and N. J. Shackleton, 1976: Variations in the Earth's orbit: Pacemaker of the ice ages. *Science*, **194**, 1121–1132.
- Held, I. M., and M. J. Suarez, 1974: Simple albedo feedback models of the ice caps. *Tellus*, **26**, 613–629.
- Imbrie, J., and K. P. Imbrie, 1979: *Ice Ages: Solving the Mystery*. Enslow Publ., Short Hills, NJ, 224 pp.
- Isaacson, E., and H. B. Keller, 1966: *Analysis of Numerical Methods*. Wiley, 541 pp.
- Jacobowitz, H., W. L. Smith, H. B. Howell, F. W. Nagle and J. R. Hickey, 1979: The first 18 months of planetary radiation budget measurements from the Nimbus 6 ERB experiment. *J. Atmos. Sci.*, **36**, 501–507.
- Jenkins, G. M., and D. G. Watts, 1968: *Spectral Analysis and its Applications*. Holden-Day, 525 pp.
- Källén, E., C. Crafoord and M. Ghil, 1979: Free oscillations in a climate model with ice-sheet dynamics. *J. Atmos. Sci.*, **36**, 2292–2303.
- Keller, H. B., 1968: *Numerical Methods for Two-Point Boundary Value Problems*. Blaisdell, 184 pp.
- Kominz, M. A., G. R. Heath, T. L. Ku and N. G. Pisias, 1979: Brunhes time scales and the interpretation of climatic change. *Earth Planet. Sci. Lett.*, **45**, 394–410.
- Kutzbach, J. E., and R. A. Bryson, 1974: Variance spectrum of Holocene climatic fluctuations in the North Atlantic sector. *J. Atmos. Sci.*, **31**, 1958–1963.
- Lamb, H. H., 1955: Two-way relationship between the snow or ice limit and 1,000–500 mb thicknesses in the overlying atmosphere. *Quart. J. Roy. Meteor. Soc.*, **81**, 172–189.
- Leith, C. E., 1973: The standard error of time-averaged estimates of climatic means. *J. Appl. Meteor.*, **12**, 1066–1069.
- Le Treut, H., and M. Ghil, 1982: Orbital forcing, climatic interactions, and glaciation cycles. Submitted to *J. Geophys. Res.*
- Libchaber, A., and J. Maurer, 1980: Une expérience de Rayleigh-Bénard de géométrie réduite: multiplication, accrochage et démultiplication de fréquences. *J. Phys.*, **41**, No. 4, C3.51–C3.56.
- Lorenz, E. N., 1963: Deterministic nonperiodic flow. *J. Atmos. Sci.*, **26**, 131–141.
- , 1970: Climatic change as a mathematical problem. *J. Appl. Meteor.*, **9**, 325–329.
- MacDonald, N., 1978: *Time Lags in Biological Models*. Springer-Verlag, 112 pp.
- Milankovitch, M., 1941: *Canon of Insolation and the Ice Age Problem*. Royal Serbian Academy, Belgrade, 482 pp. [Translated by Israel Program for Scientific Translation, Jerusalem, 1969.]
- Mitchell, J. M., Jr., 1976: An overview of climatic variability and its causal mechanisms. *Quat. Res.*, **6**, 481–493.
- Monin, A. N., and I. L. Vulis, 1979: On the astronomical theory of the earth's climatic fluctuations. *Izv. Acad. Sci. USSR, Atmos. Oceanic Phys.*, No. 1.
- Moser, J., 1973: *Stable and Random Motions in Dynamical Systems*. Princeton University Press, 198 pp.
- Namias, J., 1964: Seasonal persistence and recurrence of European blocking during 1958–1960. *Tellus*, **16**, 394–407.
- , 1978: Multiple causes of the North American abnormal winter 1976–77. *Mon. Wea. Rev.*, **106**, 279–295.
- Nicolis, C., 1982: Stochastic aspects of climatic transitions-response to a periodic forcing. *Tellus*, **34**, 1–9.
- , and G. Nicolis, 1981: Stochastic aspects of climatic transitions I. Additive fluctuations. *Tellus*, **33**, 225–234.
- North, G. R., 1975: Analytical solution to a simple climate model with diffusive heat transport. *J. Atmos. Sci.*, **32**, 1301–1307.
- , and J. A. Coakley, 1979: Differences between seasonal and mean annual energy balance model calculations of climate and climate sensitivity. *J. Atmos. Sci.*, **36**, 1189–1204.
- , L. Howard, D. Pollard and B. Wielicki, 1979: Variational formulation of Budyko-Sellers climate models. *J. Atmos. Sci.*, **36**, 255–259.
- Paltridge, G. W., 1974: Global cloud cover and earth surface temperature. *J. Atmos. Sci.*, **31**, 1571–1576.
- Parzen, E., 1961: Mathematical considerations in the estimation of spectra. *Technometrics*, **3**, 167–190.
- Rex, D. R., 1950a: Blocking action in the middle troposphere and its effect upon regional climate I. An aerological study of blocking action. *Tellus*, **2**, 196–211.
- , 1950b: Blocking action in the middle troposphere and its effect upon regional climate II. The climatology of blocking action. *Tellus*, **2**, 276–301.
- Richtmyer, R. D., and K. W. Morton, 1967. *Difference Methods for Initial-Value Problems*, 2nd ed. Wiley-Interscience, 405 pp.
- Ruddiman, W. F., and A. McIntyre, 1979: Warmth of the sub-polar North Atlantic ocean during Northern Hemisphere ice-sheet growth. *Science*, **204**, 173–175.
- , and —, 1981: Oceanic mechanisms for amplification of the 23,000-year ice-volume cycle. *Science*, **212**, 617–627.
- Ruelle, D., 1980: Strange attractors. *Math. Intelligencer*, **3**, 126–137.
- Schneider, S. H., 1972: Cloudiness as a global climatic feedback mechanism: The effects on the radiation balance and surface temperature of variations in cloudiness. *J. Atmos. Sci.*, **29**, 1415–1422.
- , and T. Gal-Chen, 1973: Numerical experiments in climate stability. *J. Geophys. Res.*, **78**, 6182–6194.
- Schutz, C., and W. L. Gates, 1974: *Global Climatic Data for Surface, 800 mb, 400 mb: October*. Rep. R-1425-ARPA, Rand Corp., Santa Monica, 192 pp. [NTIS AD 780685].
- Schwerdtfeger, W., and S. J. Kachelhoffer, 1973: The frequency of cyclonic vortices over the ocean in relation to the extension of the pack ice belt. *Antarctic J. U.S.*, **8**, 234.
- Sellers, W. D., 1969: A global climatic model based on the energy balance of the earth-atmosphere system. *J. Appl. Meteor.*, **8**, 392–400.
- Sutera, A., 1981: Stochastic perturbation and long-time climate behaviour. *Quart. J. Roy. Meteor. Soc.*, **107**, 137–151.
- Temkin, R. L., B. C. Weare and F. M. Snell, 1975: Feedback coupling of absorbed solar radiation by three model atmospheres with clouds. *J. Atmos. Sci.*, **32**, 873–880.
- Vulis, I. L., and A. S. Monin, 1979: A contribution to the astronomical theory of variations of the climate of the Earth. *Izv. Acad. Sci. USSR, Atmos. Ocean. Phys.*, **15**, 1–9.
- Winston, J. S., A. Gruber, T. I. Gray, M. S. Varadove, C. L. Earnest and L. P. Mannello, 1979. Earth-atmosphere radiation budget analyses derived from NOAA satellite data, June 1974–February 1978, Vols. 1 and 2, NOAA/NESS. [NTIS PB 80106859].